

Recent Advances in Ligand-Free, Charged and Defect-Rich Catalysts Developed by Laser Ablation and Processing in Liquids

*Dongshi Zhang, Jun Liu, Pengfei Li, Zhenfei Tian, Changhao Liang**

Dr. Dongshi Zhang, Dr. Jun Liu, Dr. Pengfei Li, Dr. Zhenfei Tian, Prof. Dr. Changhao Liang

Key Laboratory of Materials Physics, Anhui Key Laboratory of Nanomaterials and Nanotechnology, Institute of Solid State Physics, Hefei Institutes of Physical Science, Chinese Academy of Sciences, Hefei 230031, China

E-mail: chliang@issp.ac.cn, dongshi17@126.com

Keywords: Ligand-free; Laser ablation in liquids; Laser processing in liquids; Catalysis; Doping Semiconductor

Abstract

Catalysts are the foundation of sustainable and renewable energies to address the depletion of natural fossil fuels problem. Because the catalysts' activity is surface chemistry dependent, those “naked”, so-called ligand-free catalysts with more active sites exposing to the reactants are more preferable. With ligand-free, highly surface charged nanomaterials as the innate products, a newly emerging technique—laser synthesis and processing in liquids—is gaining increasing attention. The priority of laser-synthesized ligand-free metallic catalysts over chemically-synthesized counterparts has been confirmed by increasing groups through comparative studies on their catalytic activities. Besides the ligand-free metallic catalysts, this technique also excels at synthesis of bimetallic-alloy, core-shell and defect-rich semiconductor catalysts, and show good compatibility with other techniques (e.g., hydrothermal treatment and electrophoresis) to develop advanced catalysts such as ternary oxide, doped semiconductor, supported composite, nanoparticle-polymer matrix and film catalysts. Following the concept of why to choose, how to synthesize and where to use, in this review, we first introduce the advantages of this technique and the synthesized catalysts, secondly show how to develop complex catalysts using the laser-generated particles as the building blocks, and finally present the exciting application examples for photodegradation, water splitting and fuel cells.

Introduction

Catalysis is now a research hotspot in both academia and industry because of their widespread applications for developing sustainable/renewable energies to lessen the global energy crisis and for photodegrading poisonous organic molecules to reduce the environmental contamination.^[1] To meet these demands, both physical top-down and chemical bottom-up methods which enable the synthesis of nanoscale catalysts with well controlled size, morphologies and extraordinary activities are extensively exploited.^[2] However, while adopting ligand-involved wet-chemical approaches where capping agents impose adverse effects on the catalysts,^[3] the ligand removal procedure by either thermal or oxidative treatment is inevitable, during which process the chemical and physical properties of the treated catalysts can also be altered. The ligands conjugated on the catalysts are capable of blocking the active sites and result in catalyst deactivation.^[4] After two decades of development, a gradually blooming interdisciplinary technique (involving optics, nanoscience, physics and chemistry) consisting of laser ablation of bulk targets in liquids^[5] (LAL) and laser processing of colloids in liquids (LPL), has manifested itself as a facile and efficient one-step tool for nanomaterial synthesis, especially the ligand-free nanoparticle (NP) products which are very appealing for catalytic applications.

LAL is a top-down technique taking use of a pulse laser to ablate a target which is immersed in a liquid (e.g., water,^[6] ionic liquid,^[7] organic solvent,^[8] surfactant^[9] or polymer containing solution^[10] or their mixtures^[11]). At the initial state of LAL, a plasma with high temperature (3000 ~ 7000 K) and high pressure ($1.3 \times 10^5 \sim 5.7 \times 10^7$ Pa) is generated^[12] which cause atomization and ionization of the ablated materials

chinaXiv:201710.00080v1

and their ejection in liquid, leaving behind ablated grooves.^[13] During the rapid plasma quenching, its energy is transferred to the surrounding liquid and simultaneously a cavitation bubble forms which captures most of the colloids inside.^[14] The fast plasma generation-quenching process^[15] ($10^{-10} \sim 10^{-17}$ s) facilitates the production and the preservation of rich defects in the nucleated nanomaterial catalysts. After the bubble collapses, the colloids are released inside the liquid and then undergo particle coalescence,^[5d, 16] attachment,^[11, 17] or self-assembly^[18] to evolve into different types of nanomaterials, including metallic, oxide, carbide, nitride and nanoparticle-polymer composites.^[10, 15] Because LAL synthesis method is completely different from the “mild” chemical methods, novel nanomaterial with unique physical and chemical properties are anticipated and the literature published so far have confirmed this speculation, see section 2. In particular, the innate ligand-free nanomaterials generated by LAL are attractive for catalytic applications on one hand lies on the convenience which free researchers from the complicated cleaning procedures for ligand removal, including centrifugation, solvent extraction, calcination or ozonolysis, on the other hand lies on the “naked” bare surface with high activity, ruling out the blocking effect by the ligands.

LPL containing fragmentation in liquids^[16, 19] (LFL) and laser melting in liquids^[20] (LML) with the former on the basis of photothermal vaporization^[19a] or Coulomb explosion^[21] mechanisms while the latter on the basis of the laser-induced heating mechanism,^[22] is often used aiming at either narrowing the size distribution^[23] or introducing surface defects,^[24] purifying the NP phases^[25] or fusing colloidal mixtures

into alloy particles^[20a] and metal-encapsulated oxide composites^[26]. LAL-synthesized colloids,^[23, 27] chemically-synthesized NPs^[28] and microscale powders^[24, 29] are all suitable for LPL, thus ensuring the widespread applicability of LPL for tailoring the physical and chemical properties of catalysts.

The fundamental researches of LAL and LPL have undergone a rapid progress since two decades ago,^[10, 15, 30] and LAL/LPL-synthesized colloids have shown high compatibility with other methods allowing further construction/change into ternary-oxide, doped, supported, nanoparticle-polymer and film catalysts (section 3), benefitting from which and driven by the great demand for renewable and sustainable energies, the use of LAL/LPL-synthesized NPs for catalytic applications has stride forward steadily with new results coming out one by one. In this review, we tend to review the development of LAL/LPL-synthesized catalysts from the methodological point of view, and to reveal the advantages originating from these catalysts with emphasis on the diversity of achievable catalysts (e.g., alloy, core-shell, hollow, composite), ligand-free surface chemistry and surface charge of obtained catalysts, and unsaturated-coordination and oxygen vacancy introduction as well as how to use LAL/LPL-synthesized nanoparticles (NPs) to construct ternary oxide, doped semiconductor, supported composite, nanoparticle-polymer catalysts and film catalysts aiming at pointing out their integration abilities as building blocks for advanced catalysts and electrodes. Finally, representative literature showing distinguishable features of LAL/LPL-synthesized nanomaterials for catalytic applications (photodegradation, water splitting, direct methanol fuel cells and

electrochemical detection) are introduced (section 4), followed by which our perspectives on the current challenges and future trends are presented (section 5).

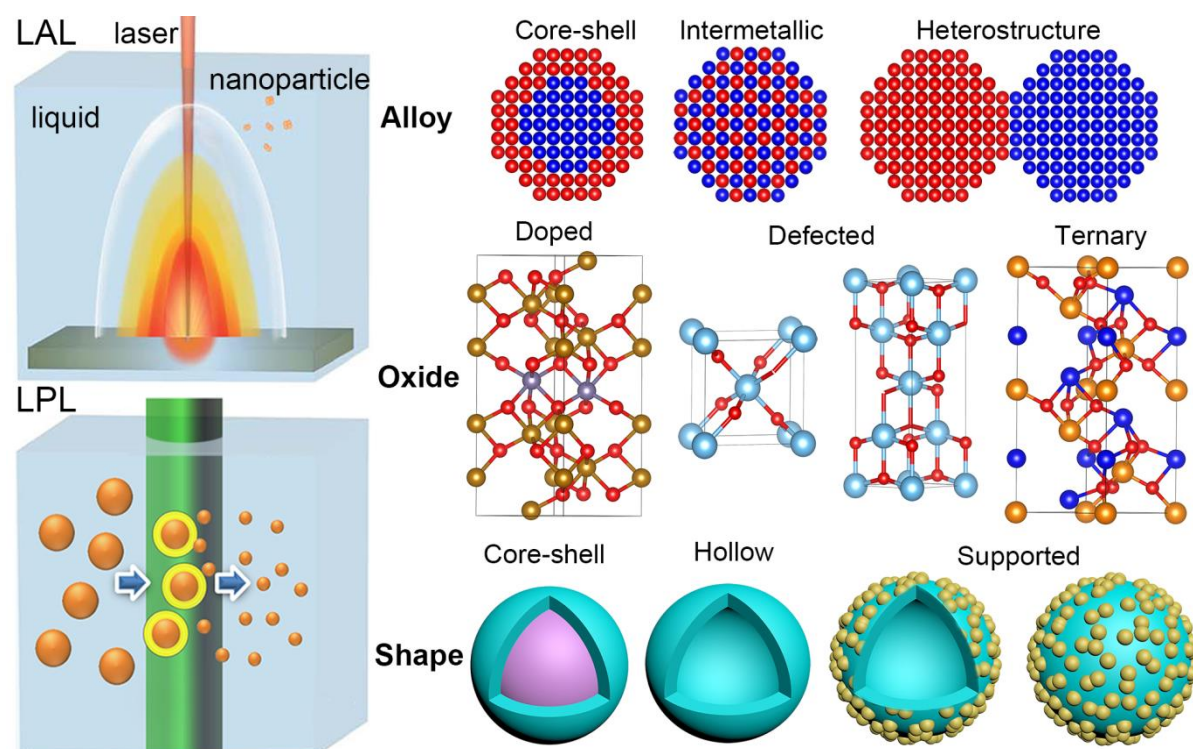


Figure 1. Schematic of LAL and LPL processes and the obtainable bimetallic-alloy (core-shell, intermetallic and heterostructure) and oxide (e.g., Ge-doped α -Fe₂O₃, anatase and rutile TiO₂, ZnSnO₄) catalysts and the typical shapes of synthesized catalysts.

Advantages of LSPC for Catalysis

Catalyst Diversity by LAL

2.1.1 Bimetallic Catalysts

Bimetallic nanoparticles, classified into three types including core-shell, intermetallic/alloyed structures and heterostructure, often outperform their monometallic counterparts while used as catalysts because of the synergistic effects

between the metals.^[31] However, synthesis of bimetallic NPs, especially alloyed NPs is very complicated and difficult,^[32] which indirectly increases their production cost and in turn hinder their extensive use in practice. LAL and LPL techniques are very convenient to transform bulk bimetallic targets (commercial^[8, 11] or self-pressed pellets using powders' mixture^[33]) and colloidal mixtures,^[20a, 34] respectively, into different kinds of bimetallic nanoparticles (Figure 2a), such as core-shell (e.g., Fe@Au,^[35] Cu@Ag^[36]), heterostructure (e.g., Cu-Ag^[37]) and alloys (e.g., AgAu^[34b, 38], PtCo,^[20a] PtFe,^[20a] PtNi^[20a]). With the diversity enrichment in the LAL-synthesized alloy NPs, many tests have been performed for the applications of laser-synthesized alloyed particles for various catalytic reactions to evaluate their activities. In 2014, Ma and coworkers confirmed the occurrence of a strong synergistic effect between Au and Pt during the 4-Nitrophenol reduction, while in comparison no synergistic effect was found while using the mixed Au and Pt NPs (Figure 2b).^[39] Later on, Oko et al. showed that Au₇₀Pt₃₀ NPs alloying derived from LAL could significantly enhance the oxidation current of ascorbic acid by three times as compared to that of Au NPs.^[40] Recently, Barcikowski group alloyed Ni with Mo into NiMo alloy NPs by LAL and demonstrated their synergistic effect on the basis of oxygen evolution reaction (OER) (Figure 2c).^[33] Surprisingly, LAL-synthesized Cu₆₃Ni₃₇ alloy nanoparticles outperform Cu, Ni and even Pt NPs as the cocatalysts with TiO₂ nanorods for photocatalytic H₂ evolution (Figure 2d).^[41] All these reports reveal the competence of LAL in producing alloy NPs. Considering the intriguing cost-effective instinct of LAL merely in need of cheap bulk targets and liquids, it can be visualized that a new

avenue towards development of various bimetallic NPs is being paved using LAL technique.

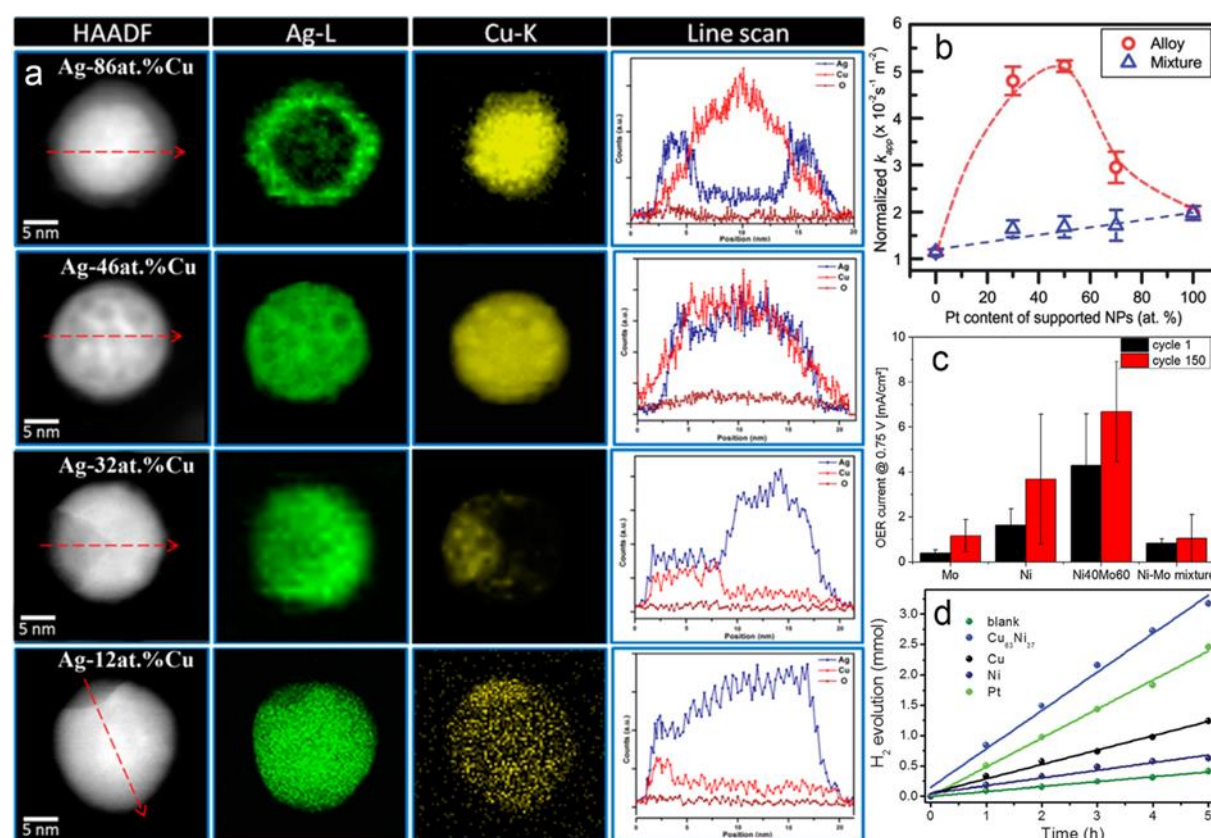


Figure 2. Bimetallic nanoparticles synthesized by LAL and their catalytic performance. (a) core-shell, intermetallic and heterostructure Ag-Cu NPs with different Cu atom ratios as determined by high angle angular dark field (HAADF), energy dispersive X-ray (EDX) mapping and line scan. Adapted from permission of Ref ^[37]. Copyright 2014 American Chemical Society. (b) Variation of the normalized k_{app} with respect to the Pt content in Pt_xAu_{100-x} alloy-NP/ CeO_2 -NTs. Adapted from permission of Ref ^[39]. Copyright 2014 Royal Society of Chemistry. (c) Comparison of the OER activity of Mo, Ni and $Ni_{40}Mo_{60}$ alloy colloid as well as a 40:60 mixture of nickel with molybdenum colloid. Adapted from permission of Ref ^[33]. Copyright 2016 Elsevier. (d) Typical time courses of H_2 evolution in the systems with different

cocatalysts. Reprinted from permission of Ref ^[41]. Copyright 2017 Royal Society of Chemistry.

2.1.2 Core-Shell Catalysts

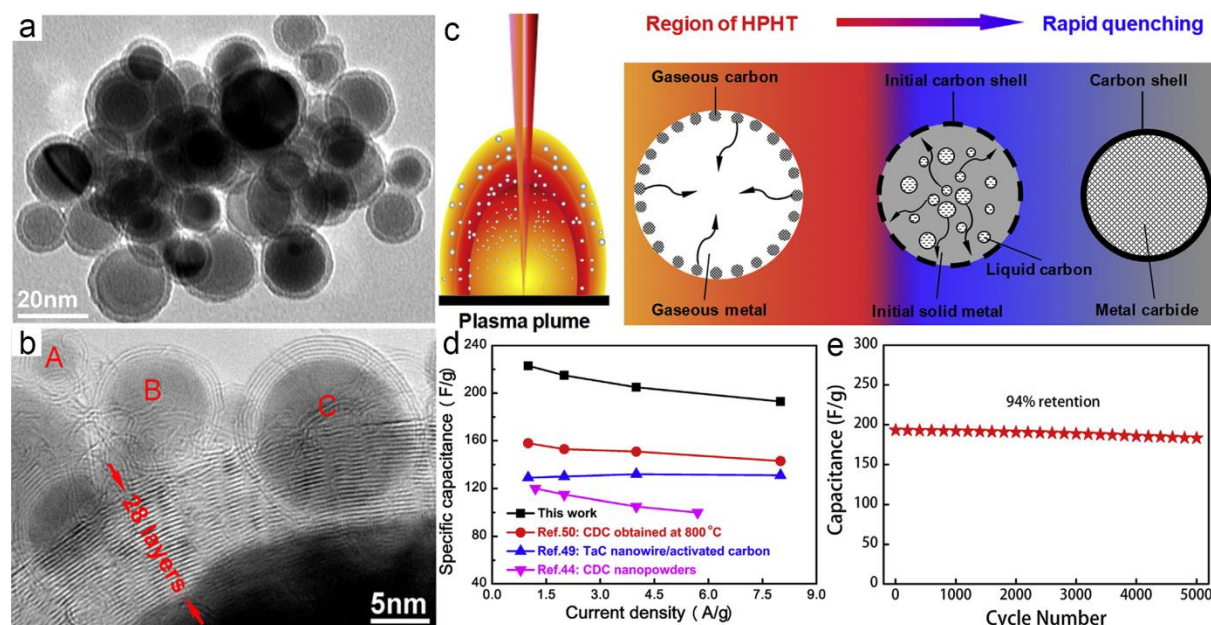


Figure 3. Formation of inorganic@carbon core-shell particles and their catalytic applications. (a, b) Low and high-resolution TEM images of LAL-synthesized inorganic@carbon core-shell particles. (c) Schematic illustration for the formation process of C-coated core/shell NPs. (d) Comparison of the specific capacitance of TaC@C core-shell NSs with other recently reported carbide-derived carbon and TaC nanowires/activated carbon. (e) Cycling performance of TaC@C core-shell NSs. Reprinted with permission from ref ^[42]. Copyright 2013 Elsevier. Reprinted with permission from ref ^[43]. Copyright 2016 Elsevier.

The type of core-shell NPs is a prevailing catalysts because the shell-coating enables to improve the NPs' stability and dispersibility and lessen the reactivity decrease of

core particles during catalytic experiments.^[44] Among various shell candidates, carbon shell is of great interests due to its high chemical and thermal stabilities,^[45] thus making the carbon-coated core-shell particles very appealing for electrochemical applications. It has been widely reported that carbon shell is an inborn feature while implementing LAL in organic solvents (Figure 3a).^[42-43] This is because of the fact that laser generated plasma is so powerful enough to decompose organic molecules into carbon clusters which would rapidly precipitate and coalesce on the formed inorganic NPs during the rapid plasma quenching (Figure 3c).^[43] To date, a large variety of carbon-coated core-shell NPs have been synthesized by LAL, such as TaC@C,^[43] NbC@C,^[43] HfC@C,^[43] MoC@C,^[43] W₂C@C,^[46] Au@C^[47] and Co₃C@C.^[42] The onion shell has as high as 28 carbon layers (Figure 3b).^[42] Some of these LAL-synthesized carbon-coated particles have already shown their potential as supercapacitor electrode materials for energy storage, such as a specific capacitance up to 223 F g⁻¹ (Figure 3d) and a slight loss of capacitance (< 6%) after 5000 charge discharge cycles (Figure 3e) were obtained while using LAL-TaC@C assembled electrodes.^[43]

2.1.3 Hollow Catalysts

Core-shell NPs are good sacrificial templates to synthesize hollow catalysts by the dissolution method, in which concept the core materials should be susceptible to acids while the shell materials should be resistant to acid etching. Hollow particles like ZnS cages^[48] have been successfully achieved using an acid-containing solution for LAL to trigger in situ etching of Zn-core. Selective etching of LAL-synthesized Zn@ZnO

core-shell NPs into hollow Zn core^[49] suggested that hollow ZnO should be also accessible by LAL of Zn targets in acid solutions. Many other metal@oxide core-shell particles (e.g., Fe@FeO_x,^[50] FeMn@FeMn₂O₄,^[11] AuFe@FeO_x^[51]), although have been developed by LAL, yet no endeavor has been devoted to transforming them into hollow structures by in situ selective etching LAL.

2.1.4 Composite Catalysts

With the considerations of either to enhance the catalysts' stability or to prevent electron-hole recombination or to lower the costs of anode and cathode catalysts, many efforts have been devoted to decorating catalysts on supports with high specific surface areas, high porosities, high electric conductivities, high thermal and mechanical stabilities, such as oxides^[52] (e.g., TiO₂, Al₂O₃, SiO₂, CeO₂) and graphene-derivative layered structures.^[53] Traditional techniques (e.g., precipitation and impregnation) and newly emerging techniques (e.g., melt infiltration, colloidal synthesis atomic layer deposition) are the widely adopted approaches to the synthesis of supported catalysts.^[52] As compared to these complicated techniques, LAL provides a one-step platform to allow spontaneous attachment of the target-ejected materials to the solid support additives in liquids, termed as in situ LAL synthesis of supported catalysts, differing from the ex situ synthesis of supported catalysts realized by subsequent colloids mixing (section 3.3). To date, layered structures (e.g., graphene^[54] or graphene oxide^[55] (GO)) and particle colloids (e.g., Al₂O₃,^[56] CeO₂,^[57]) have been utilized for in situ construction of supported catalysts. With defined adsorbent colloidal solution, simply changing the target composition and then

comparing the resultant catalytic difference induced by adsorbate alternation (e.g., $\text{Al}_2\text{O}_3\text{-AgAu}$, $\text{Al}_2\text{O}_3\text{-Ag}$) allow flexibly and fastly selecting the optimal adsorbate.^[56] In addition, benefiting from highly charged surfaces, LAL/LPL-obtained stable NPs are easily to be assembled into supported catalysts through mixing them with the oppositely charged support colloids or into film catalysts by electrophoretic deposition (EPD) for device development (section 3.5).

Ligand-Free Surface Chemistry

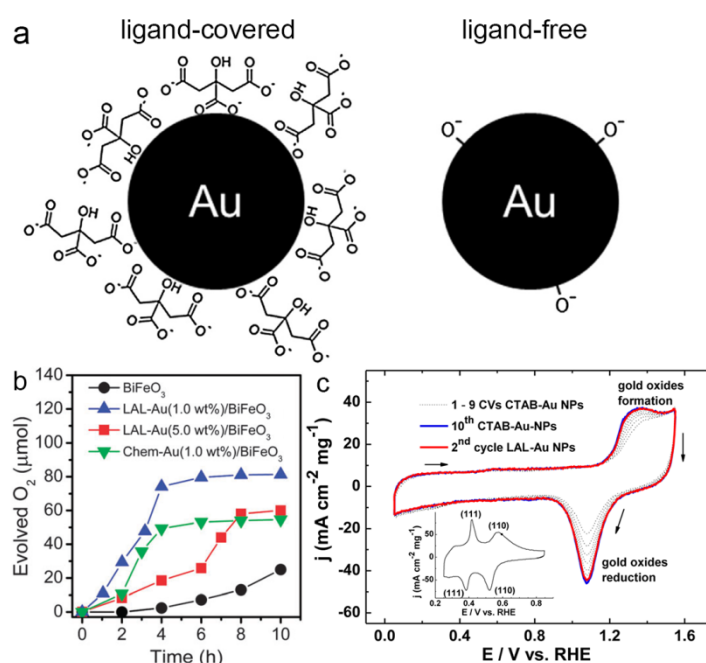


Figure 4. Surface chemistry and catalytic reactivity comparison between chemically-synthesized ligand-covered counterparts and LAL-synthesized ligand-free Au NPs. (a) surface chemistry of citrate-covered and LAL-synthesized ligand-free Au NPs. Reprinted with permission from ref ^[58]. Copyright 2013 Elsevier. (b) Oxygen evolved upon visible light ($\lambda > 380 \text{ nm}$) illumination of the FeCl_3 suspension (4 mmol L^{-1} , 50 mL) containing the photocatalysts (50 mg) of LAL-Au/ BiFeO_3 and

Chem-Au/BiFeO₃ NPs, respectively. Reprinted with permission from ref ^[59].

Copyright 2013 Royal Society of Chemistry. (c) Cyclic voltammograms (CV) of the Au electrodes formed by LAL-Au NPs and chemically synthesized CTAB-Au NPs in 0.1 mol L⁻¹ NaOH recorded at 20 mV s⁻¹ and at a controlled temperature of 20 °C. The inset shows the underpotential deposition of lead in 0.1 mol L⁻¹ NaOH and 1 mmol L⁻¹ Pb(NO₃)₂ for a LAL-Au NPs-based electrode under the same conditions. Reprinted with permission from ref ^[60]. Copyright 2015 American Chemical Society.

Normally, most chemically-synthesized particles are covered by ligands^[58] (Figure 4a, left) or stabilizers which to some content change the intrinsic activity of the as-prepared catalysts, sometimes even leading to the catalytic deactivation.^[4] In terms of no influence of surface-impurity, LAL-synthesized ligand-free particles^[58] (Figure 4a, right) are anticipated to be good reference materials for both theoretical studies on kinetics of catalytic reactions and to experimentally enhance the catalytic reactivities. And the findings reported so far has indeed confirmed theses hypothesis. For the theoretical modelling, a strong support is the higher fitting rate (70% fitting^[61]) of LAL-synthesized Au NPs than the chemically-synthesized polyelectrolyte-brush covered Au NPs (30% fitting^[62]) to Langmuir–Hinshelwood model based on the reduction reaction of 4-nitrophenol into 4-aminophenol. For the experimental verification, a strong support is the remarkably higher reaction rate constant of LAL-synthesized AuNPs ($1.40 \times 10^{-2} \text{ s}^{-1} \text{ m}^{-2}$) over Chem-AuNPs ($2.25 \times 10^{-2} \text{ s}^{-1} \text{ m}^{-2}$) tested as adsorbants on CeO₂ adsorbent supports for reaction of 4-nitrophenol.^[63] Moreover, Li et al. demonstrated that the photocatalytic activity of LAL-synthesized

Au NPs is 1.5 times of chemically-synthesized Au NPs (Figure 4c) by respectively assembling same amount (1.0 wt%) of BiFeO₃ nanowires for water oxidation.^[59] Hebié et al. showed that the 2nd Cyclic Voltammogram (CV) cycle of the electrodes assembled by LAL-Au NPs for glucose electrooxidation is equal to the 10th cycle of the electrodes prepared by cetyltrimethyl ammonium bromide (CTAB)-Au NPs (Figure 4d) thus proving higher electrochemical activity of LAL-Au NPs over chemically-synthesized CTAB-Au NPs.^[60] Hence, it can be envisaged that LAL-synthesized ligand-free metallic catalysts with more active sites are excellent substitutes of ligand-covered catalysts to further promote the catalytic performance.

Surface Charge

Zeta potential (ζ -potential) is often used to identify whether a colloidal solution is stable or not. In general, when the measured zeta potential of a colloid is above 30 mV or below -30 mV, the colloid is stable because the repulsive forces among the charged NPs are strong enough to keep them well dispersed.^[64] Table 1 lists the zeta potential of various NPs obtained by either LAL or LPL, including Au,^[65] Ag,^[66] Cu,^[66] Mg,^[66] Pd,^[7] Ge,^[5d] TiO₂,^[67] ZrO₂,^[66] and Au@SiO₂.^[68] To help researchers know how these colloids are synthesized and what their physical states are, synthesis conditions and particle size are included. It is clear that most metallic particles synthesized in water are negatively charged. Sylvestre et al. confirmed that it is the M-O⁻ and M-OH⁻ bindings on the particle surfaces that induce surface charges to stabilize Au NPs.^[65d] Through measuring the zeta potential of LAL-synthesized ZnO NPs with pH adjusted by HCl and NaOH addition, He et al. revealed that the surface

states are actually pH-dependent with MOH_2^+ appearing at low pH while M-O^- forming at high pH.^[69] Besides acids and alkalis, ionic buffers are also capable of adjusting the strength of NP surface charges, in which field Barcikowski group did a lot of works.^[7, 70] They found that zeta potential of the LAL-synthesized particles are ionic strength^[7] (1~10 mM) and ion type^[71] ($\text{F}^- \approx \text{SO}_4^- < \text{Cl}^- \approx \text{NO}_3^- < \text{I}^- \approx \text{Br}^- \approx \text{SCN}^-$) dependent, hence concluded that ion adsorption plays an important role in the stability of the LAL-synthesized colloids.^[70] Detailed effects of ions and pH environments on the colloidal nanoparticles can refer to a review published by Pfeiffer et al.^[72] To obtain positively charged metal particles, cationic surfactant CTAB is a good additive, in which case CTA^+ ions first neutralize the negatively charged particles and then gradually attach to the particle surfaces to form a double-layer coating and result in the stable particles.^[73] No matter whether the colloids are negatively or positively charged, they are long-term stable to be either directly used or mixed with the oppositely charged supports to form supported composite catalysts (section 3.3), or assembled into film catalysts by EPD (section 3.5). Of great significance, it is the surface charges that rule out the ligand-requirement like the wet chemical synthesis method thus allowing one-step convenient synthesis of NP catalysts, and it is also the surface charges that make the synthesized NPs “naked” enough to allow them exposure of more active sites to the reactants for sufficient reactions, which can well explain the higher activities of LAL-synthesized catalysts over chemically-synthesized counterparts shown in section 2.2.

Table 1. Zeta potential and particle size of LAL/LPL-synthesized NPs under different synthesis conditions.

Method	Materials	Zetal potential	Particle size	Synthesis conditions (targets, laser properties, ablation period, liquids)	Ref.
LAL	Ag, Cu, Mg, ZrO ₂	−40 mV	Majority <10 nm	Bulk targets; Laser (< 10 ps, 1030 nm, 200 kHz, 250 μJ/pulse); 30 s ablation; 50 ml acetone	[66]
LAL	Au	−30 mV	20-80 nm	A metal plate; Nd:YAG (10 ns, 1064 nm, 10 Hz, 90 mJ/pulse); 20 min ablation; 20 mL of water	[65a]
LAL	Au	−49 mV	9-12 nm	Nd:YAG (8 ns, 1064 nm, 10 kHz, 385 μJ/pulse); 3 min ablation; 30 mL of water	[74]
LAL	Au	−24 ~ −47 mV	5-40 nm	A gold rod; Ti:sapphire (120 fs, 800 nm, 1 kHz, 0.2 mJ/pulse); 20 min ablation; 3 mL deionized water, or NaCl, KCl, NaNO ₃ , HCl (0.1 N solution in water), NaOH (0.1 N solution in water)	[65d]
LAL	Au	−28 mV (in water) +32 ~ +40 mV (in CTAB)		A gold disk; Ti:sapphire (100 fs, 800 nm, 1 kHz, 300 μJ/pulse); 20 min ablation; 2mL of either aqueous solution of CTAB or pure deionized water	[65b]
LAL	Pd	0~−81 mV	3.4 nm	A Pd target; Nd:YAG laser (9.8 ps, 1064 nm, 1064/532, 100 kHz and 126μJ/pulse); 3 min ablation; Milli-Q water, sodium phosphate, sodium carbonate, odiumhydroxide	[7]
LAL	Ge	−83 mV	7-8 nm	A Ge target; Nd:YAG laser (10 ns, 1064 nm and 100 mJ/pulse); 5 min ablation; 15 mL deionized water	[5d]
LAL	TiO ₂	−45 mV	~23 nm	A titanium target; Nd/YAG laser (8ns, 1064 nm, 10 Hz, 120 mJ/pulse); 20 min ablation; 20 mL of deionized water	[67a]
LAL	ZnO	−45 ~ +30 mV	15~26 nm	A Zn plate; Nd/YAG laser (7 ns, 355 nm, 10 Hz, 100 mJ/pulse); 60 min ablation;	[69]

LAL	Au@SnO ₂	-38 mV	16±4 nm	HCl (pH 5.36) and NaOH (pH 11.98) A Au target; Nd: YAG laser (10 ns, 1064 nm, 10 Hz, 60 mJ/pulse); 10 min ablation; 10 mL of SnCl ₄ aqueous solution (0.1 M)	[68]
LPL	Au	-37 ~ -65 mV	12~30 nm	1.5 mg/3.0 mL Au (99.9%) flakes with a nominal thickness of 0.1-0.2 μm; Nd:YAG laser (6 ns, 1064/532 nm, 10 Hz, 40 and 100 mJ/pulse); 60 min irradiation; in either Air or Ar or O ₂ atmosphere	[65c]
LPL	TiO ₂	-50 mV	6±3 nm	10 mg/mL anatase-TiO ₂ powder; Nd:YAG laser (6 ns, 1064 nm, 10 Hz); 60 min irradiation; acetone	[67b]
LPL	TiO ₂	-59 mV	30 nm	10 mg/mL rutile TiO ₂ powder; Nd:YAG laser (6 ns, 10 Hz, ~1 J/(pulse cm ²)); 10 min; deionized water	[67c]

Unsaturated-Coordination and Oxygen Vacancy Introduction

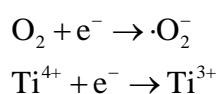
Metal-oxide semiconductor nanomaterials are good candidates as photocatalysts,^[1b] whose applicable scope relies on their bandgap and surface defects. It is also acknowledged that surface oxygen defects behave like unpaired electrons. The extra electrons in the vacancies act as donor-like states and create an accumulation layer in the near-surface region, may cause a downward band bending, a band flattening or even an upward band bending.^[75] Also, surface-defect induced bandgap bending affects the efficiency of light absorption and therefore influence the photocatalytic activity^[76] and the adsorption or the desorption of reactants or product molecules.^[77]

LAL and LPL have proven to be skilled at one-step synthesis of defect-rich, especially oxygen-vacancy-rich oxides (e.g., TiO_x,^[24, 67c, 78] SnO_x,^[79] x < 2) which can be used as dopants to develop doped catalysts (e.g., (Ge, Si, Mn, Sn or Ti)-doped

α -Fe₂O₃^[80], section 3.2) or allow in situ reduction of metal ions to develop supported catalysts (e.g., Ag-TiO₂,^[67a] SnO₂-rGO^[81] (reduced graphene oxide), section 3.3)

In this section, we take use of TiO₂ as a representative to show how oxygen-vacancies are introduced by LAL/LPL. Because the Ti/O ratio is 2 for stoichiometric TiO₂, there will be 6 oxygen vacancies in 10 TiO₂ molecules when atomic ratio of Ti/O is 1:1.4.^[67a] In general, the presence of oxygen vacancies is often accompanied by the presence of Ti³⁺. For convenience, researchers often use Ti³⁺ concentrations to indirectly characterize the density of oxygen vacancies.

Both X-ray photoelectron spectra (XPS) and electron paramagnetic resonance (EPR) spectrum have confirmed the presence of Ti³⁺ in the LPL-prepared TiO₂ colloids.^[67c] XPS spectrum shows that the binding energy peaks at 458.9 and 464.7 eV of Ti⁴⁺ (2p_{3/2} and 2p_{1/2} core levels) belonging to pristine TiO₂ educts shift to 458.2 and 462.5 eV after laser irradiation which fit well with the 2p_{1/2} and 2p_{3/2} core level of Ti³⁺, respectively. Additionally, the presence of Ti³⁺ induces an apparent EPR signal, while in comparison, no signal is observed for the pristine TiO₂ educt. It is considered that during LPL, high-energy laser (e.g., $h\nu = 3.49$ eV) triggers an electronic transition between conduction and valence bands of TiO₂ which are Ti 3d and O 2p states, respectively. O atoms donate the electrons, while Ti⁴⁺ accepts the electrons to form Ti³⁺, following the reactions shown below.^[78] After the O atoms are peeled off from the TiO₂ NP surface, oxygen vacancies form.



Through calculating the ratio of Ti^{3+} peak areas to overall Ti^{3+} and Ti^{4+} peak areas in XPS spectra, the Ti^{3+} content can be roughly speculated. The highest ratio of $\text{Ti}^{3+}/(\text{Ti}^{3+}+\text{Ti}^{4+})$ atomic ratio is as high as 49%, which was obtained by LPL of rutile TiO_2 powder in deionized water (concentration: 10 mg/mL) using a ns Nd:YAG laser (6 ns, 355 nm, 10 Hz, $\sim 1 \text{ J}/(\text{pulse cm}^2)$) for 10 mins.^[67c]

When it comes to LAL, the formation mechanism of Ti^{3+} is different. The percentage of Ti^{3+} in the (TiO_2 : Ti^{3+}) products is laser-energy dependent with the maximal value of 45.45%.^[82] The authors proposed that the plasma-related thermodynamic state and rapid quenching process play a critical role in the formation of TiO_2 with different ratios of Ti^{3+} . Specifically, with increasing the laser energy, a relatively higher thermodynamic state forms during LAL and more Ti_5O_9 NPs are produced which will be frozen due to the rapid quenching of plasma plume. Further increasing laser energy will increase the quenching time and as a result, increases the transition opportunities from metastable state of Ti_5O_9 to stable TiO_2 state. A large number of Ti^{3+} and oxygen vacancies in the LAL/LPL-obtained TiO_2 NPs are favorable to enhance the photocatalytic performance towards degradation of organic molecules (section 4.1) and hydrogen generation through water splitting (section 4.2).

Downstream Extension using LAL-Synthesized Colloids

To enrich the diversity of achievable catalysts, enormous efforts have been put to upgrade the LAL/LPL-synthesized NPs into highly advanced catalysts, such as ternary oxide, doped catalysts, supported catalysts, nanoparticle-polymer composites and film

catalysts for catalytic applications in combination with various techniques, including hydrothermal treatment, colloidal solution mixing, polymerization and EPD. In this section, the advance in these complex catalysts with the LAL/LPL-synthesized NPs as building blocks is introduced. Apart from the advanced catalysts presented below, LAL-synthesized colloids are as well able to be constructed into core-shell-NP supported catalysts (e.g., Fe@C/Pd construction starting from LAL-obtained Fe@C colloids for m-dichlorobenzene degradation^[83]) and capsule-like catalysts (e.g., Au-encapsulated ZnO nanospheres for selective gas sensing^[26]).

Ternary Oxide

Ternary oxides, also known as binary metal oxides, containing at least one transition metal ion and one or more electrochemically active/inactive ions possess the synergistic effects of their composed oxides and have been widely exploited for catalytic applications, such as supercapacitors^[84] and Li ion batteries.^[85] Synthesis of ternary oxides is feasible by thermal treatment which utilizes high temperature and high pressure to dissolve materials and recrystallize the resultant products, also applicable for LAL-obtained colloids. Often, a solution containing active oxide precursors which enables chemical reactions during thermal treatment has to be prepared in advance. There are two options for precursor solution preparation. One is successive LAL of different targets in the same solution. For example, to synthesize Zn₂GeO₄ NPs, LAL can be first implemented to a Zn target in water. After LAL, the Zn target is replaced by a Ge target while keeping the fresh colloid still in the chamber. After a period of LAL, the solution contains both highly active Zn and Ge

precursors.^[86] The other option is to mix the precursor colloids obtained by separate LAL of each target and then implement the hydrothermal treatment. This method is more favorable than the successive LAL method because (1) it is easy to control and characterize the precursor colloids, (2) the weight ratios between the precursor colloids can be flexibly and accurately adjusted. In 2012, Tian et al. first reported the successful synthesis of zinc stannate using LAL-obtained $\text{ZnO}_x(\text{OH})_y$ and SnO_x colloidal precursors and manipulated their phase and morphology (e.g., cube-like Zn_2SnO_4 and urchin-like ZnSnO_3) by adding different concentrations of ammonia (Figure 5a-e).^[87] These ternary oxide photocatalysts display good photocatalysis decomposition performance towards methyl orange (MO) and 2,5-dichlorophenol (2,5-DCP), as shown in Figure 5f-g. Inspired by this work, different kinds of ternary oxides have been developed by hydrothermal treatment of LAL-synthesized colloid precursors, including PbSnO_3 ,^[88] Zn_2GeO_4 ,^[86] NiCo_2O_4 ,^[86] Zn_2SnO_4 ,^[86] ZnFe_2O_4 ,^[86, 88] NiFe_2O_4 ,^[88] ZnMnO_3 ,^[86] Fe_2GeO_4 ,^[86] AgVO_3 ,^[88] BiOCl ,^[89] Bi_2WO_6 ,^[89] and BiVO_4 .^[89] Also, hydrothermal treatment allows the precursors to react with particle additives to form ternary-oxide containing composites and therefore the functions of the products are enriched. For example, introducing magnetic-field responsive Fe_3O_4 @C in the LAL-induced Zn and Sn colloidal precursors allows the formation of chestnut-like Fe_3O_4 @C@ ZnSnO_3 catalysts (Figure 5h) after hydrothermal treatment, which can be recycled after photocatalytic reactions with the assistance of an external magnetic field (Figure 5i-j).^[90]

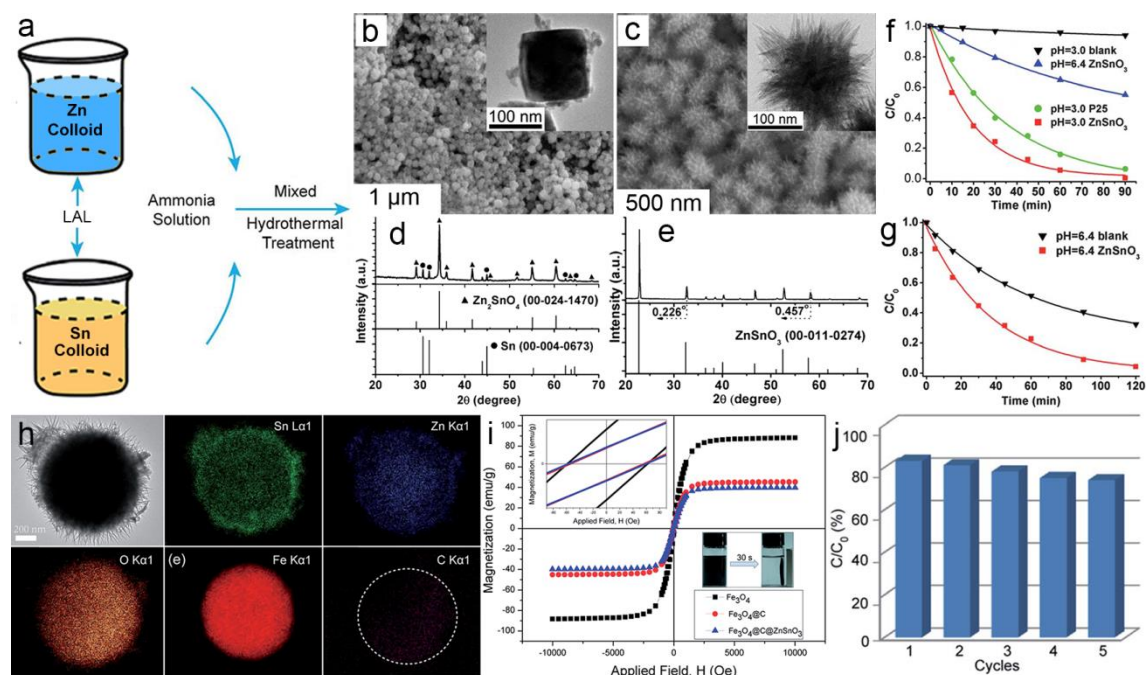


Figure 5. Ternary oxide synthesis. (a) Preparation route for synthesizing zinc stannate nanostructures by LAL, colloids mixing and hydrothermal treatment. (b-e) SEM/TEM images and XRD of as-synthesized zinc stannate nanostructures with different amounts of ammonia added: (a, c) 0 mol/L and (b,d) 3.0 mol/L. (f-g) Photocatalysis decomposition of MO and 2,5-DCP, respectively. (h) TEM image and EDX mapping of a single Fe₃O₄@C@ZnSnO₃ core-shell particle. (i) Magnetization hysteresis loops of Fe₃O₄, Fe₃O₄@C, and Fe₃O₄@C@ZnSnO₃ measured at room temperatures. (j) Cycle evaluation of the photocatalytic removal of 2,5-DCP over the core-shell Fe₃O₄@C@ZnSnO₃ particles. Reprinted with permission from ref ^[87]. Copyright 2012, ref ^[90]. Copyright 2014 Royal Society of Chemistry.

Doped Catalysts

Doping catalysts with elements (e.g., Si, Ge, Sn, Ti, Nb, Cr, Zn, etc) to modify their optical and electrical properties is one widely adopted strategy for performance enhancement, especially attractive for the potential commercial catalysts with the properties of low cost, abundance, nontoxicity, and stability, such as hematite ($\alpha\text{-Fe}_2\text{O}_3$).^[91] After several years' investigation, LAL-synthesized precursor colloids have manifested themselves appropriate as the dopants for doped-catalyst development.^[80, 92] Liang's group pioneered this field and has successfully doped Ge, Si, Mn, Sn and Ti elements in $\alpha\text{-Fe}_2\text{O}_3$ by hydrothermal treatment of FeCl_3 ions and LAL-synthesized colloids following the mechanism shown in Figure 6a.^[80] First, $\alpha\text{-Fe}_2\text{O}_3$ nuclei form upon hydrothermal treatment with the precursors of FeOOH . Simultaneously, H^+ ions are released in the solution which will dissolve the LAL-obtained $\text{MO}_x(\text{OH})_y$ -like clusters ($\text{M} = \text{Ge, Si, Mn, Sn, and Ti}$) and as a result, stable M^{n+} ions (e.g., Ge^{4+} , Si^{4+} , $\text{Mn}^{2+}/\text{Mn}^{3+}$, Sn^{4+} , and Ti^{4+}) are generated. They will participate in $\alpha\text{-Fe}_2\text{O}_3$ NPs during their growth leading to the formation of doped $\alpha\text{-Fe}_2\text{O}_3$ NPs with dopant-determinant morphologies (Figure 6a). Besides the composition, dopants' concentration also influences the morphology of the as-prepared $\alpha\text{-Fe}_2\text{O}_3$ nanomaterials. For example, 2% Ge-doped $\alpha\text{-Fe}_2\text{O}_3$ turn out to be circular nanosheets with a diameter of about 250 nm and a thickness of about 10 nm, while 5% Ge-doped $\alpha\text{-Fe}_2\text{O}_3$ come up with hexagonal nanosheets (average aspect size about 200 nm and a thickness of about 10 nm), both of which differ from the undoped hematite $\alpha\text{-Fe}_2\text{O}_3$ cubes and parallelepipeds (Figure 6b-d).^[92a] It is noteworthy that dopants are not always randomly distributed in $\alpha\text{-Fe}_2\text{O}_3$. Under

optimized conditions, dopants (e.g. Ge) are able to distribute in the hematite lattice in an ordered manner to form superlattice structures.^[92a] As expected, Ge-doped hematite $\alpha\text{-Fe}_2\text{O}_3$ show better photoelectro-chemical (PEC) performance than undoped hematite, as indicated by the maximal photocurrent density on different applied potentials.

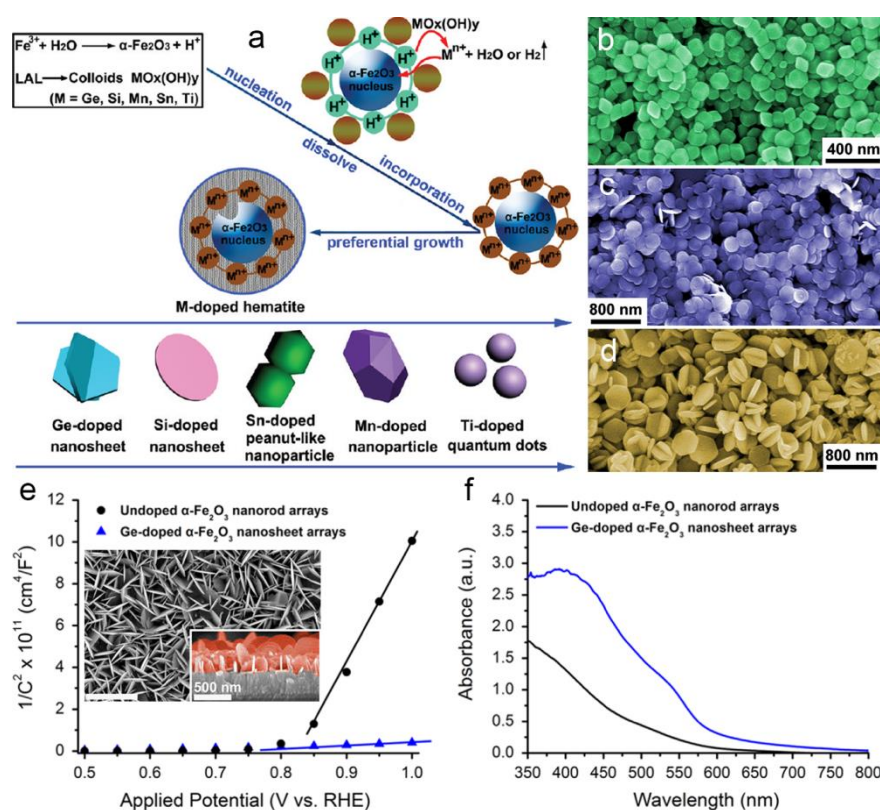


Figure 6. Doped catalysts synthesis and their catalytic performance. (a) Schematic of the doping process and the resulting doped-hematite nanocrystals. Reprinted with permission from ref ^[80]. Copyright 2012 American Chemical Society. (b-d) Typical SEM images of undoped, 2% Ge-doped, and 5% Ge-doped $\alpha\text{-Fe}_2\text{O}_3$. Reprinted with permission from ref ^[92a]. Copyright 2013 Elsevier. (e-f) Mott-Schottky plots and UV-vis optical absorption spectra of undoped $\alpha\text{-Fe}_2\text{O}_3$ nanorod arrays and Ge-doped

α -Fe₂O₃ nanosheet arrays with annealing temperature of 550 °C. Inset image shows the high magnification SEM image of Ge-doped α -Fe₂O₃ nanosheet arrays. Reprinted with permission from ref ^[93]. Copyright 2014 Elsevier.

Solution-drying of colloids to prepare hematite photoanodes often results in a disorder doped nanocrystals' stacking. The spatial gap between the photoanode materials and the underlying conductive substrate generally generates a large interface impedance and hinders the carrier collection and transport seriously. One solution to this problem is by constructing a direct path, such as an array of single-crystal nanostructures on the conductive substrate, to facilitate electron transport to the conductive substrate and the photogenerated holes to the catalyst-electrolyte interface, respectively. Then a question arise regarding how to assembly hierarchical nanostructure anodes using LAL-obtained precursor colloids with the assistance of hydrothermal treatment. As mentioned above, FeOOH is the precursors of α -Fe₂O₃.^[80] It is reasonably to construct FeOOH-structure films on the conductive substrates (e.g., fluorine-doped tin oxide coated glasses) then immerse these films inside LAL-obtained colloidal precursor solutions followed by hydrothermal treatment to construct hematite nanostructure arrays photoanodes.^[93-94] Liu et al. reported that Ge-doped α -Fe₂O₃ nanosheet arrays prepared by this method have a higher carrier density (Figure 6e) and absorption efficiency (Figure 6f) than that of the undoped α -Fe₂O₃ nanorod arrays and show a remarkable photocurrent density of 1.4 mA cm⁻² at 1.23 V vs. RHE,^[93] about tenfold of the performance using the pure α -Fe₂O₃ nanorod arrays anodes.^[92a] As seen, a new approach to synthesis of doped α -Fe₂O₃ in the manner of either colloids or solid

structures has been paved on the basis of LAL-synthesized precursor colloids. Although there is no comparative study regarding whether LAL-colloids are more favorable than chemically-synthesized counterparts as dopants for catalytic applications. The above mentioned works indeed verify the possibility and demonstrate the potential of using LAL-synthesized precursor colloids as dopants. But so far the host catalyst is limited to α -Fe₂O₃, future researches should be done toward diversifying the matrix of dopants and the host materials and exploiting the optimal combination for different catalytic purposes.

Supported Catalysts

To prevent the agglomeration of the catalysts during reactions, anchoring catalysts on inert supports is often implemented.^[52] Charge-driven adsorption on the basis of electrostatic interactions between the adsorbent supports and adsorbate (metal or oxide) catalysts is an easy strategy to construct supported catalysts, which has been widely investigated using innate LAL-synthesized charged particles, such as the formation of NYF@TiO₂-Au,^[95] Au-BiFeO₃^[59] and MWCNT-ZnO^[96] for photocatalytic applications, Au/CeO₂ for CO oxidation^[63] and Au-TiO₂ for oxidation of ethanol.^[97] Higher adsorption efficiency is preferable because in this case more active sites of catalysts are possible to participate in the catalytic chemical reactions. Wagener et al. reported that ligand surface coverage of the particles plays a dominant role in the adsorption efficiency.^[98] Completely ligand-free metal NPs and low ligand-coverage NPs allow Freundlich adsorption, while those particles covered by citrate ligands with surface coverage no less than 50% are unavailable for NP

adsorption on microparticle supports because of electrosteric repulsion induced by ligand shells (Figure 7a-b). As shown in section 2.3, most of the LAL-produced metal (e.g. Au) particles are negatively charged, they have high affinity to the positively charged supports, such as CeO₂ nanotubes. Therefore, almost 100% immobilization of AuNPs on the surface of the CeO₂ nanotubes (20 mg) was observed within 30 min.^[63]

To ensure the maximal adsorption efficiency, searching for the Isoelectric Point (IEP) of the catalysts' and supports' colloidal solutions is indispensable. IEP is the pH value where the colloids have no net electrical charges, often determined by measuring zeta-potential values of the colloids by varying the pH of the colloidal solutions and the ionic strength of the NPs. Marzun et al. reported that there exists a process “window” for sufficient adsorptions while considering both ionic strength and pH values, as marked by blue color in Figure 7c-d.^[99] Ionic strength should be controlled in a range to ensure the colloidal stability, while the pH value should lay between IEP of the support (IEP-TiO₂ = 6.3) and IEP of the particles (IEP-Pt= 2.8) to facilitate the electrostatic attraction between the supports and the particles. During the adsorption process, a net-charge transfer from the NPs to the support takes place and results in the IEP shift toward the NP IEP (IEP-(Pt-TiO₂) = 5.0). If the electrostatic interaction adjusted by pH and ionic strength is sufficient enough, the inhibition effect of NP surface-ligands (citrate, polyvinylpyrrolidone (PVP) and lipoic acid (LA)) on adsorption will be weakened or even prevented, thus presenting an avenue to improve the adsorption efficiency of ligand-coated NPs. As shown in Table 1, most of the colloids synthesized by LAL/LPL are charged enough to stabilize themselves. Even

though the surface charges are in the unstable range of $-30 \text{ mV} \sim 30 \text{ mV}$, using pH and ionic solutions to strengthen the NP surface charge also ensure no contamination by ligand additives, thus ruling out the possibility of active-site shielding occurring during the adsorption process.

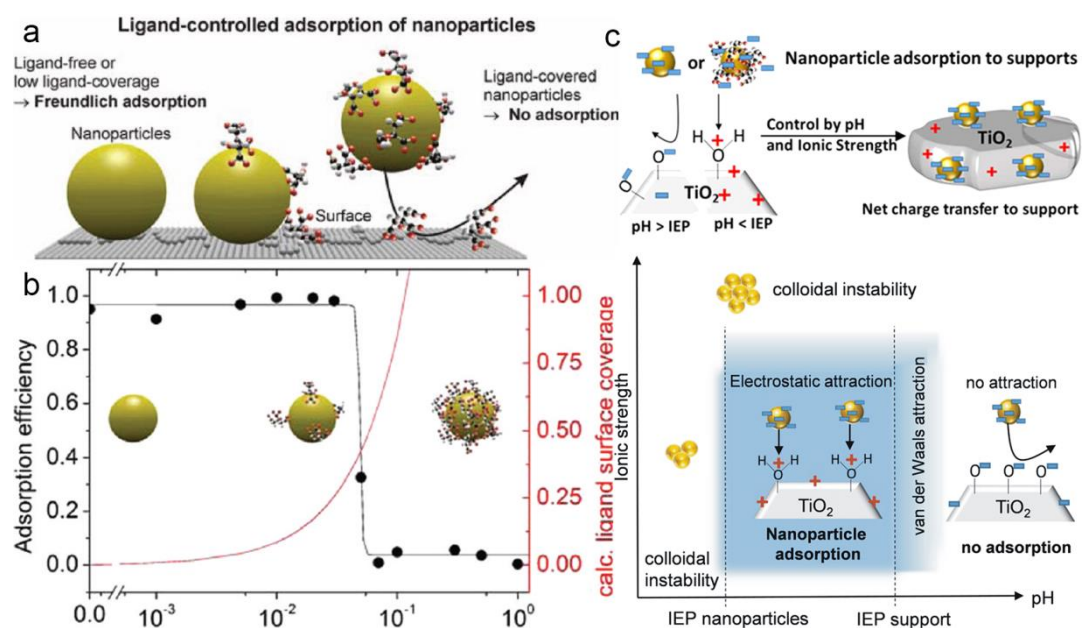


Figure 7. Adsorption process to construct supported catalysts. (a) Sketch of adsorption process of NPs due to their surface coverage. Microparticles covered with ligand-free NPs (left) and unaffected microparticles after mixing with ligand-stabilized NPs (right). Reprinted with permission from ref ^[98]. Copyright 2012 American Chemical Society. (c) schematic of Pt-TiO₂ adsorption efficiency controlled by pH and ionic strength. (d) Scheme of nanoparticle adsorption to supports as a function of pH and ionic strength. Reprinted with permission from ref ^[99]. Copyright 2014 American Chemical Society.

chinaXiv:201710.00080v1

New paths of synthesizing supported catalysts have also been paved by in situ reduction of the LAL-produced non-stoichiometric oxides (e.g., SnO_x , TiO_x) through the hydrothermal treatment or the aging method. For example, Zhang et al. successfully developed Ag- TiO_2 composite catalysts using LAL-obtained defect-rich TiO_x colloids to reduce Ag^+ ions for photodegradation of pentachlorophenol, which substantially enhanced the degradation rate of LAL-obtained TiO_x fresh colloids from 60% to 98% after 160 min UV irradiation.^[67a] Ye et al. showed that the abundant electrons, surface hydroxyls and defects of LAL-synthesized SnO_x colloids can attack the oxycarbon atoms of GO and resulted in the formation of stable SnO_2 -rGO composites, the electrode made by which allows non-enzymatic electrochemical sensitive detection (sensitivity of $1.93 \text{ A M}^{-1} \text{ cm}^{-2}$) of trace amount of glucose molecules (the detection limit of $13.35 \mu\text{M}$).^[81]

Nanoparticle-Polymer Catalysts

Nanoparticle-polymer composites have gained increasing attention due to their combined functions coming from NPs and polymers, respectively. Zhang et al. recently summarized the in situ and ex situ laser prototyping approaches to developing various NP-polymer composites as well as the downstream techniques for further function extension of in situ/ex situ synthesized NP-polymer colloidal composites.^[10] As for the catalytic application, one representative work from Ma group deserves introduction because it shows the potential of polymer encapsulated LAL-synthesized particles for multiple-functional catalyst development.^[100] They grafted thiol-terminated PDEAEMA (SH-PDEAEMA) on LAL-synthesized Au NPs

chinaXiv:201710.00080v1

to develop a CO₂-switchable and in situ recyclable catalysts.^[100] Since the Au NPs are naked without any ligands coating, it is easy to perform surface grafting by SH-PDEAEMA and the steady Au–sulfur bonding ensures the stability of the synthesized PDEAEMA–AuNPs colloids. The PDEAEMA–AuNPs can undergo reversible dispersion upon CO₂–N₂ purging. CO₂ purging makes the colloids well disperse, while N₂ purging make the colloids become aggregated. The performance of PDEAEMA–AuNP and LAL–AuNP catalysts after several reaction cycles’ reduction of 4-NP. As seen, the PDEAEMA–AuNPs by CO₂–N₂ purging shows a much higher catalytic activity as compared to LAL–AuNPs after first round, which is attributed to the less severe aggregation of PDEAEMA–AuNPs than LAL–AuNPs during sample recycling by the centrifugation process.^[100] Moreover, deducing from the identical catalytic activity of PDEAEMA–AuNP and LAL–AuNP catalysts in the first round, it can be speculated that polymer grafting does not block the active sites of Au NPs. This is of great importance from the viewpoint of catalytic applications where the main concern is the catalytic performance. It is anticipated that with advance of further excavation of the polymer diversity applicable for NP grafting or encapsulation, polymer functionalization of LAL-synthesized catalysts will offer more choices to flexibly manipulate the laser-synthesized catalysts.

Film Catalysts

To develop electrochemical devices, assembling colloids into film catalysts (electrodes) is indispensable. Considering LAL-synthesized colloids are highly charged, directly transforming them into film catalysts can be easily realized by EPD.

Multiple devices have been successfully fabricated along this route, including solar cells,^[101] neural electrodes,^[102] biosensor electrode,^[103] environmental detector's electrode^[104] and electrochromic films.^[105] One advantage of using laser-synthesized ligand-free particles for EPD has been revealed by Streich et al.^[74] They found that highly electrophoretic mobile LAL-obtained ligand-free NPs allow controllable barrier-free deposition with linear deposition rate, while in contrast, ligand-coated NPs only allow certain amount of materials' deposition.^[74] Without any other effect in the particle-to-film process chains other than the system factors (e.g., voltage, particle concentration and charge, etc.), the highly active sites of LAL-synthesized NPs are well preserved after being transforming into film catalysts, which is of great importance for sufficient electrode-electrolyte-interface reactions to take place.

If adopting magnetic particles, magnetophoretic deposition becomes possible. Drop-casting of LAL-synthesized NPs (e.g., FeO_x) onto a substrate (e.g., ITO-coated glass) and put a magnet below the glass slide till the colloidal solution completely evaporate to form a particle-film electrode.^[106] Generally, a coarse electrode surface with uneven NP distribution turns out and the film will be susceptible to mechanical scratch because the NPs only physically stack together.

Catalytic Applications

Due to low cost, long life span, high energy power density, good reversibility, and pollution-free operation, electrochemical devices have gained tremendous interests as future sustainable and renewable energy suppliers and as well been widely investigated using LAL/LPL-obtained electrochemical catalysts such as gas

sensing,^[26, 107] biosensor,^[81, 103] detection of heavy metal ions,^[104] biofuel cells,^[60] supercapacitors.^[108] While adopting metallic NPs as electrode materials, the naked NP surface property is considered to play the dominant role, which have been introduced in section 2.2. Hence, in the following, we mainly focus on the capacities and the underlying reasons of the reported excellent photocatalysts for photodegradation and water splitting. Additionally, a few LAL-/LPL-synthesized catalysts with highly commercial potential for fuel-cell applications are also presented as compared to the currently commercial products of P25 and Pt/C.

Photodegradation

Organic and heavy metal contaminants have caused severe environmental problems that pose threats to natural species and human beings and hence arouse wide concerns in destroying these pollutants. As an environmental-friendly and cost-effective method, photodegradation using semiconductor photocatalysts is deemed as a good choice which has been an active area for decades.^[1b] A large variety of photocatalysts have been developed by either LAL or LPL or their combination with downstream techniques (e.g., hydrothermal treatment) for photodegradation of organic molecules (e.g., methylene blue (MB), methyl orange (MO), 2,5-dichlorophenol (2,5-DCP),) or heavy metal ions (e.g., $K_2Cr_2O_7$), including TiO_2 ,^[24, 109] SnO_x ,^[79b] ZnO ,^[49a] α - Ag_2WO_4 ,^[110] $ZnSnO_3$,^[87] $Sn_6O_4(OH)_4$,^[111] $Fe_3O_4@C@ZnSnO_3$,^[88] $Ta_xO@Ta_2O_5$,^[112] TiO_2/Ti_5O_9 ,^[82] ZnO/TiO_2 ,^[113] Pt/ZnO ,^[49b] $MWCNT/ZnO$,^[96] $ZnTiO_3/TiO_2$,^[114] Au/CeO_2 ,^[63] Sn_2S_3 ,^[115] ZnS/Zn ^[48] and titanate nanostructure.^[116]

Given the difference in the composition of photocatalysts and the targeted degraded molecules as well as the difference in the concentrations of adopted photocatalysts, conclusions can not be made for which photocatalysts are the most favorite ones, especially for LAL-synthesized photocatalysts. The results summarized in Table 2 can serve as a reference to help guide future investigations in this field from the methodology viewpoint.

Table 2. Photodegradation of different organic molecules and ions using LAL-synthesized and LPL-obtained nanomaterials.

Method	Materials	Catalytic experimental conditions	Performance	ref
LAL	5nm $\text{Sn}_6\text{O}_4(\text{OH})_4$	5 ml of 100 mg l^{-1} fresh $\text{Sn}_6\text{O}_4(\text{OH})_4$ colloid solution is added to 10 ml of 15 ppm MO aqueous solution	97% reduction rate of MO after 25 min irradiation	[111]
LAL	$\text{Ta}_x\text{O}@ \text{Ta}_2\text{O}_5$ (10–40 nm)	3 mg photocatalysts were added into 1.8 ppm (15 mL) MB aqueous solutions	92% degradation rate of MB after ca. 40 min UV- light irradiation	[112]
LAL	$\text{Ti}_5\text{O}_9\text{-TiO}_2$ (10–15 nm)	5 mg photocatalysts were dispersed in a 10 mL aqueous solution of Rh.B with a concentration of 10 mg L^{-1}	Almost complete oxidation of rhodamine B after 180 min visible-light irradiation	[82]
LAL	TiO_2 (a.v. 34 nm)	20 μl of MB solutions (0.05 wt.%) was added to the titanium oxide dispersion with 100 $\mu\text{g/ml}$	90% degradation rate of MB after ca. 180 min UV- light irradiation	[109a]
LAL	SnO_x (a.v. 30 nm)	5 mg SnO_x powders were added in 30 mL of 25 mg L^{-1} MO aqueous solution (pH = 3.0)	Almost complete degradation rate of MO after 150 min UV light irradiation	[79b]
LAL	PVP-encapsulated rutile TiO_2 (a.v. 55 nm)	20 mg TiO_2 NPs was added in methylene blue (1.0×10^{-5} M, 40 ml) aqueous solution.	Almost complete reduction of MB after 300 min irradiation using UV light	[109d]
LAL+ etching	ZnS/Zn nano-cage, ZnS@Zn core-shell NPs (30~50 nm)	2.7 mg ZnS/Zn NPs was added into 10 mL of 1×10^{-2} M aqueous $\text{K}_2\text{Cr}_2\text{O}_7$ solution.	99.9% reduction rate of Cr(IV) using ZnS/Zn nano-cages after 20 min light irradiation	[48]
LAL+ etching	Sn_2S_3 (sub-10 nm size, porous)	10 mg Sn_2S_3 porous was added in 50 ml of 1×10^{-3} M Cr(vi) aqueous solution.	99.8% degradation rate of Cr(VI) after 8 min visible light irradiation	[115]

LAL+ ultrasonic irradiatio n-assisted two-step etching	Pt/ZnO (20 nm, Pt 1.1 nm)	10 mg catalyst powders were added into 10^{-5} M (20 mL) MO aqueous solution	90% degradation rate of MO after 40 min UV-light irradiation	[49b]
LAL+ Hydrother mal	ZnSnO ₃ (urchin-like, 200 nm)	30 mg L ⁻¹ NPs were added in 30 mL of MO aqueous solution (25 mg L ⁻¹ , pH of 3.0)	98% degradation rate of MO after 90 min and 95% of the 2,5-DCP after 120 min UV-light irradiation	[87]
LAL+ Hydrother mal	Hierarchical titanate spheres 150– 250 nm	3 mg titanate spheres were added in 30 mL of PCP solution (concentration of 20 mg L ⁻¹ and pH of 3)	99% degradation rate of PCP in 240 min under the UV-light irradiation	[116]
LAL+ Hydrother mal	Fe ₃ O ₄ @C@Z nSnO ₃ (a.v. 600 nm)	the dried Fe ₃ O ₄ @C@ZnSnO ₃ powder (4.5 mg) was added in 20 mL of 2,5-DCP aqueous solution (15 ppm)	87% degradation rates of 2,5-DCP using core-shell Fe ₃ O ₄ @C@ZnSnO ₃ NPs	[90]
LAL+ Hydrother mal	ZnFe ₂ O ₄ , ZnFe ₂ O ₄ – rGO	3 mg photocatalysts were mixed with 35 mL 12 ppm MB solution in a 50 mL with 0.6 mL hydrogen peroxide solution (H ₂ O ₂ , 30 wt%) addition	Illuminated by a 500 W xenon lamp, nearly 50% photodegradation rate of MB after 300 min using pure ZnFe ₂ O ₄ NPs while 99.5% photodegradation rate using the ZnFe ₂ O ₄ –rGO NCs	[88]
LAL+ Mixing	NYF@TiO ₂ – 1 wt% Au core@shell microspheres (a.v. 500 nm)	10 mg of the NYF@TiO ₂ –Au were added to 10 mL of MO solution (20 mg L ⁻¹)	96% photodegradation rate of MO after 60 min UV-light irradiation	[95]

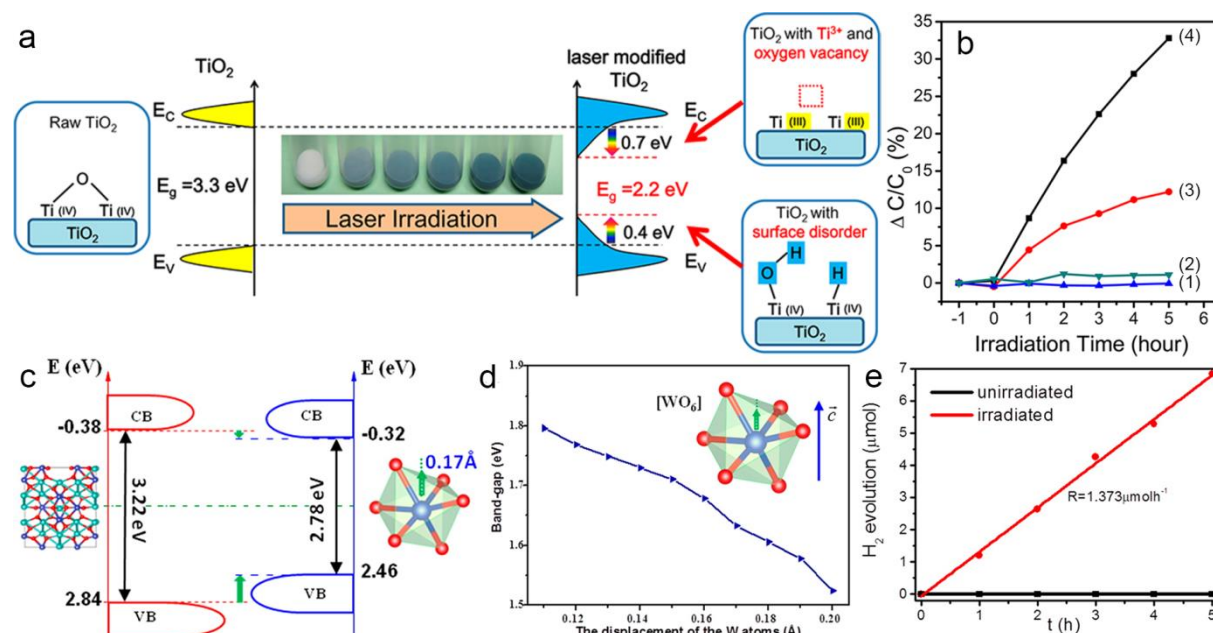


Figure 8. Photocatalytic activity enhancement due to the modified surface state after LPL. (a) Schematic illustration of electronic density states of TiO₂ before and after laser modification together with the optical images of the counterparts. From left to right: raw TiO₂, TiO₂-5 min irradiation, TiO₂-15 min irradiation, TiO₂-30 min irradiation, TiO₂-60 min irradiation, and TiO₂-120 min irradiation. (b) Photocatalytic degradation curves of rhodamine B under irradiation of a green LED ($\Delta C/C_0$ vs irradiation time): (1) P25, (2) raw TiO₂, (3) TiO₂-60, and (4) TiO₂-120. Adapted with permission from ref ^[24]. Copyright 2015 American Chemical Society.

As for the competence and potential of LPL technique for photodegradation purposes, TiO₂ photocatalysts are used as the representative for clarification because TiO₂ is the most studied and used photocatalysts due to its low cost, high activity, nontoxicity, long-term chemical and thermal stability. Now, TiO₂ P25 containing w.t.71% of anatase and w.t.29% of rutile which enables to enhance the adsorption capacity of reactants and increase the density of both lattice defects and carrier, is used as a benchmark to evaluate the activity of lab-made synthesized photocatalysts. Chen et al. compared the performance of photocatalytic degradation of rhodamine B using P25 and LPL-obtained TiO₂ NPs as well as the pristine raw unirradiated TiO₂ NPs with the results shown in Figure 8a-b.^[24] As seen, P25 and pure TiO₂ NPs with band gap of 3.3 eV are unable to degrade rhodamine B under visible light, while LPL-obtained TiO₂ NPs show an increased photo-degradation efficiency towards rhodamine B. And the higher time the TiO₂ NPs are irradiated, the more active the as-prepared TiO₂ catalysts become (3-4 curves in Figure 8b). Through analyzing the surface states of

the LPL-obtained TiO₂ NPs, they concluded that the surface lattice disorder, including Ti–H and O–H bonds, induces a blue-shift (0.4 eV) of valence band maximum of TiO₂, while Ti³⁺ or oxygen vacancy cause a shift of conduction band position by 0.7 eV (Figure 8a). Therefore, the bandgap (2.2 eV) of the LPL-prepared TiO₂ catalysts is 1.1 eV less than those of unirradiated TiO₂ (3.3 eV), leading to a drastic enhancement of photocatalytic performance. It has been confirmed that Ti³⁺ or surface oxygen can give rise to midgap bands close to the conduction band (CB) minimum and introduce a vacancy-induced band^[117] and enable an enhanced absorption of sub-bandgap light.^[76] In analogy to Ti³⁺ or surface oxygen vacancies, large amounts of lattice disorder in TiO₂ NPs may cause the yield of midgap states, which overlap with or get close to the valence band (VB) edge and thus induce the blue-shift of VB edge. The electronic reconstruction (0.87 eV band reduction caused by 30.64% Ti³⁺) still works while constructing LAL-synthesized TiO_x NPs into heterogeneous supported photocatalysts (e.g., TiO₂-GO).^[78] Yang's group discovered LPL-induced electronic reconstruction phenomenon is as well applicable to α-Ag₂WO₄ whose defect density is increased by a factor of 2.75 and band gap is reduced from 3.22eV to 2.78eV after LPL (Figure 8c), resulting in a greatly enhanced visible-light photodegradation activity and H₂ evolution (Figure 8e).^[110] On the basis of First-Principles calculation, they theoretically proved the possibility of band gap reduction induced by the structural distortion from the displacement of the W atom in the [WO₆] cluster (Figure 8d). As seen, the increase in the defect density of semiconductor oxide photocatalysts by either LAL or LPL and their resultant band gap reduction are favorable for

promoting their photocatalytic activities, which in turn, will promote the extension of LAL/LPL to other oxide photocatalysts.

Water Splitting/Oxidation

Catalytic splitting of pure water into H₂ and O₂ ($2\text{H}_2\text{O(l)} \rightarrow 2\text{H}_2\text{(g)} + \text{O}_2\text{(g)}$, $E^0 = -1.23$ V) through both oxygen and hydrogen evolution reactions (OER and HER) by either photocatalysts and electrocatalysts is currently a popular topic around the globe because the water educt is almost inexhaustible while the hydrogen product is considered to be a next-generation energy carrier for renewable and sustainable energy-related applications.^[118] Many material scientists focusing on LAL and LPL have stepped into this field trying to reveal the advantages of using laser-synthesized catalysts. In section 4.1, it has been shown that electronic reconstruction and bandgap reduction of TiO₂ photocatalysts can be induced by modifying particles' surface states (Ti³⁺, oxygen vacancy, surface disorder) using LPL technique.^[24] Hence, it is expected that other than photodegradation of organic molecules, hydrogen generation rate of water splitting using LPL-obtained TiO₂ photocatalysts should be also promoted compared to P25. Compagnini group recently did a comparative research on the photocatalytic performance of the unirradiated and the laser-irradiated P25, rutile and anatase TiO₂ and found that adopting laser-irradiated photocatalysts indeed enhanced the productivity of hydrogen gas, up to 30 mmol g⁻¹ h⁻¹ H₂ productivity, almost twice enhancement as compared to the unirradiated counterparts.^[119] Considering the nanosecond laser they used for TiO₂ treatment which inevitably led to the formation of undesirable TiO₂ big submicrospheres. Further enhancement of the

LPL-obtained TiO_2 photocatalysts' activity is anticipatable by adopting picosecond and femtosecond lasers as irradiation resources with negligible melting behaviors to minimize the catalyst dimensions.

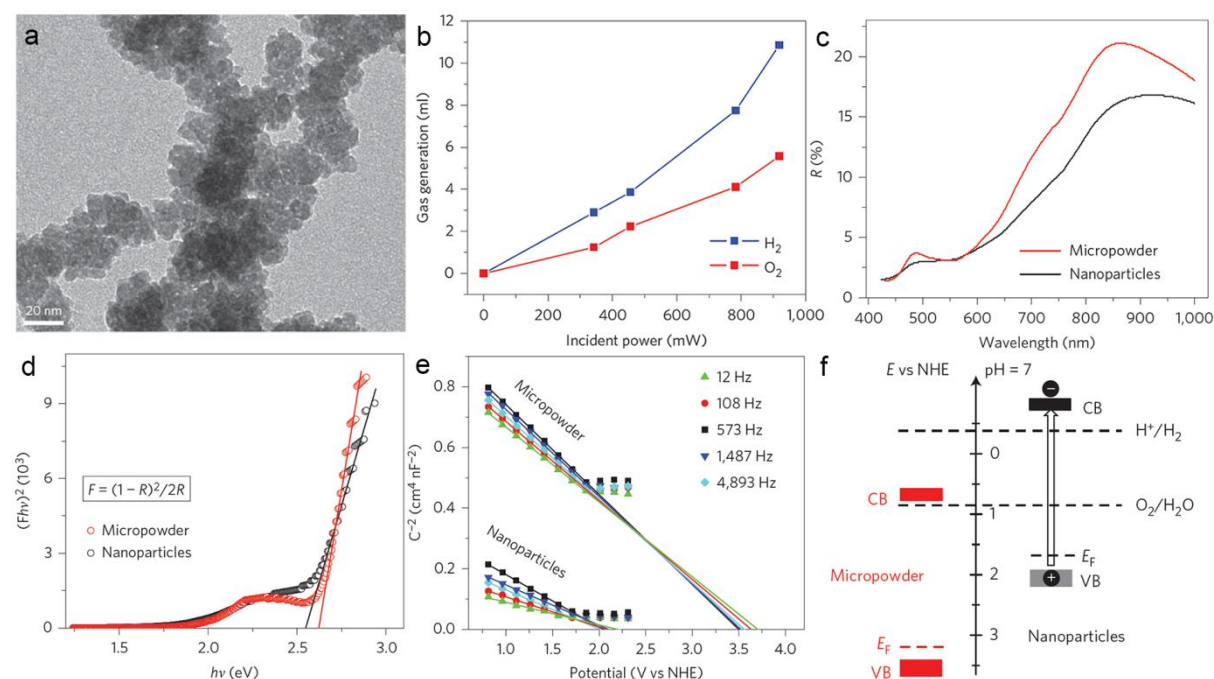


Figure 9. Band gap reconstruction triggered by LPL. (a) TEM image of LPL-obtained CoO nanoparticles, (b) Production of hydrogen and oxygen from CoO nanoparticles (~12 mg) as a function of incident laser power, (c) Ultraviolet–visible diffuse reflectance spectra of CoO nanocrystals and powders, (d) $(Fhv)_2$ as a function of photon energy ($h\nu$), where F is the Kubelka–Munk function of the diffuse reflectance R . The intercepts of extrapolated straight lines give the corresponding direct bandgaps of CoO nanocrystals and powders. (e) Mott–Schottky plots for CoO nanocrystals and micropowders according to impedance measurements. The flat-band potentials are obtained from the intercepts of the extrapolated lines. (f) Band positions of CoO nanocrystals and micropowders according to the bandgaps and flat-band potentials

obtained from figure e. CB, conduction band; VB, valence band. Reprinted with permission from ref ^[120]. Copyright 2014 Nature Publishing Group.

Ultrasmall catalysts are in priority over large catalysts because they have larger surface to volume ratios, allowing more active sites of the catalysts at the same weight exposure to the reactants as well as enabling alteration of the CB/VB band positions of photocatalysts. Liao et al. found that CoO micropowders are unfeasible for water splitting because the CB edge position (depicted according to the bandgaps and flat-band potentials shown in Figure 9f, respectively) is below the hydrogen-evolution potential.^[120] Surprisingly, the CB edge can be elevated above the hydrogen-evolution potential after downsizing CoO micropowders into nanocrystals by LPL (deduced from reflectivity spectra in Figure 9b-c and flat-band potential in Figure 9d), which in combination with VB band edge of CoO nanocrystals below oxygen-evolution potential offers an opportunity for water splitting (Figure 9b) with solar-to-hydrogen efficiency up to ~5%. In similarity, Blakemore et al. showed the possibility of reducing Co micropowders into Co₃O₄ NPs by long-period (1h) LAL in water.^[121] Such Co₃O₄ particles are as small as ~2.5 nm and do not have any ligand shielding, hence presenting a good electrocatalytic water-oxidation performance with overpotential of 314 mV (measured at 0.5 mA cm⁻²) and high mass activity of more than 10 A m⁻² g⁻¹ at 500 mV overpotential.^[121] The overpotential of a redox reaction refers to a potential above the thermodynamic potential required to overcome reaction barriers (a given turnover frequency or current density in electrocatalysis).^[122] Evaluation of catalytic activities on water oxidation ($2\text{H}_2\text{O}(\text{l}) \rightarrow \text{O}_2(\text{g}) + 4\text{H}^+ + 4\text{e}^-$), a

half reaction of water splitting, is also widely investigated because it requires the coupling of four electron and four-proton transfer to transform water into hydroxyl radical (OH^\bullet). The catalysts with excellent catalytic performance for water-oxidation are always excellent robust candidates for water splitting. Hu et al. showed that the electrocatalytic activity (mass activity of 0.28 mA/mgPt and specific activity of 1.18 mA/cm²) of LAL-synthesized PtCo alloy NPs is 2- and 5-times higher than those of commercial Pt/C (0.09 mA/mgPt and 0.19 mA/cm²).^[123] Hence, novel commercial Pt/C substitutes are anticipatable for LAL-synthesized Pt alloys. Moreover, Hunter et al. reported one of the ever reported lowest overpotential value (260 mV at 10 mA cm⁻²) for water oxidation using the LAL-obtained [Ni-Fe]-layered double hydroxides (LDHs) $[\text{Ni}_{1-x}\text{Fe}_x(\text{OH})_2](\text{NO}_3)_y(\text{OH})_{x-y} \cdot n\text{H}_2\text{O}$.^[124] These works demonstrate that the oxide, alloy and hydroxide products of LAL and LPL are excellent catalysts for water splitting.

Direct Methanol Fuel cells

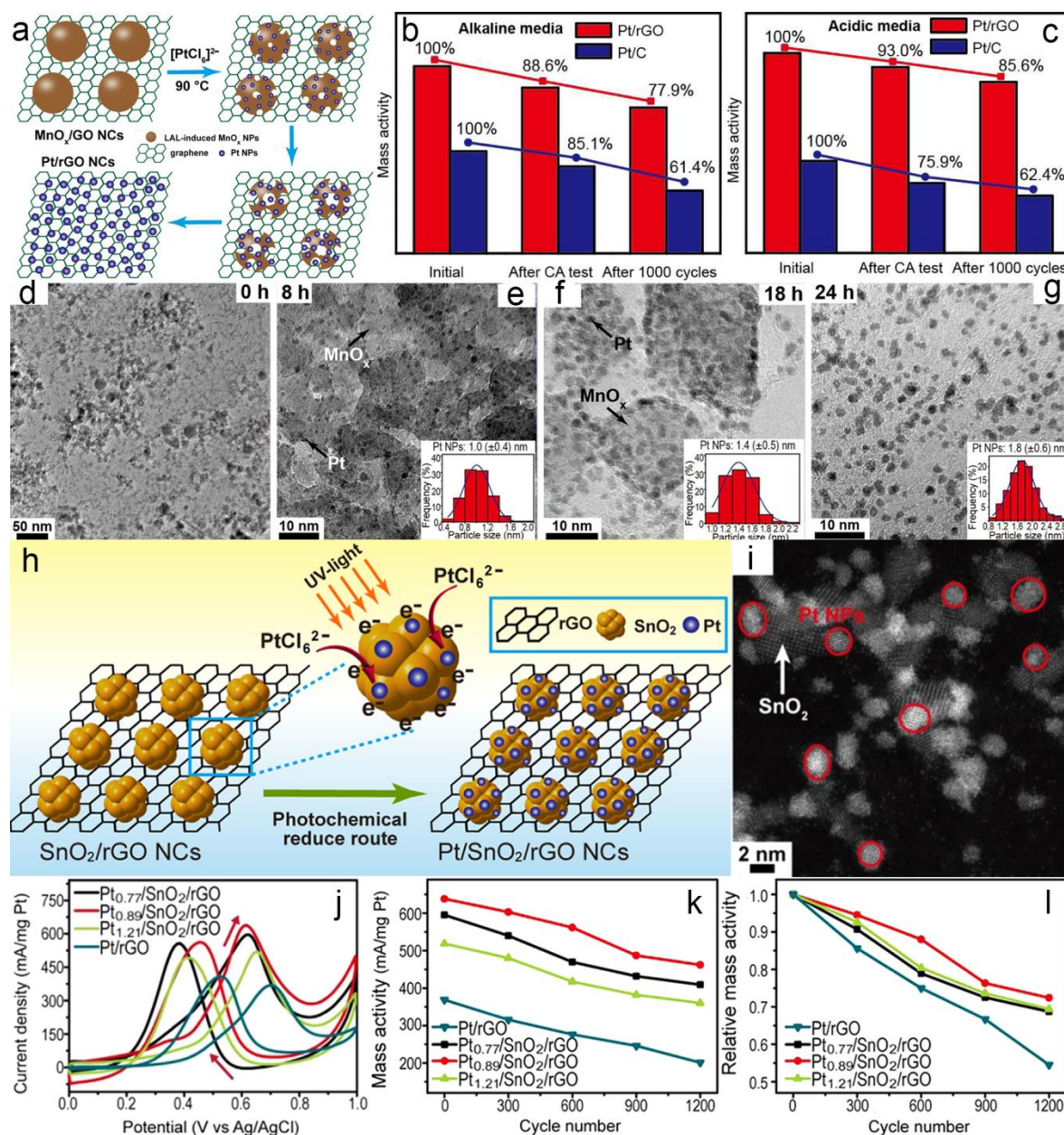
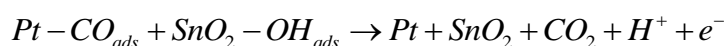
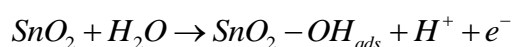


Figure 10. Direct methanol fuel cell assembled using LAL-obtained NPs. (a) Schematic Illustration for the formation of Pt/rGO NCs. (b) Mass activities of Pt/rGO and commercial Pt/C catalysts measured in alkaline (0.5 M KOH + 0.5 M CH₃OH) and acidic media (0.5 M H₂SO₄ + 0.5 M CH₃OH) initially, after CA test, and the subsequent 1000 cycles. (h) Illustration for the synthesis of Pt/SnO₂/rGO hybrid ternary nanocomposites. (d-g) TEM images of the reacted suspension colloids at different reaction intervals. Adapted with permission from ref ^[125]. Copyright 2016

American Chemical Society. (i) HAADF-STEM images of the prepared Pt_{0.89}/SnO₂/rGO nanocomposites. (j) CV curves of GC electrodes modified with prepared catalysts measured at a scan rate of 50 mV s⁻¹. (k-l) Mass activities and the normalized peak current densities at different cycle numbers for the prepared catalysts. Reprinted with permission from ref ^[126]. Copyright 2016 Elsevier.

Miniaturized fuel cells have been a research hotspot for many years to meet the increasing demand of portable electronic devices. In terms of the simple structure, high power densities, high energy conversion efficiencies, and low operation temperatures, direct methanol fuel cell (DMFC) based on the reaction of methanol oxidation into water and carbon dioxide to generate electricity is a good power source.^[127] As the core component of DMFCs, anode electrocatalysts are of great importance, for which purpose Pt-based materials are widely exploited and commercial Pt/C composites are used as a benchmark for evaluating the performance of newly developed electrocatalysts. Wu designed and achieved Pt/reduced-graphene-oxide (rGO) nanocomposites electrodes showing superior electrocatalytic activity over commercial Pt/C composites (Figure 10a-c).^[125] The LAL-obtained MnO_x colloids which are easily dissolved in acid solutions are used as sacrificial templates for in situ reduction of PtCl₆²⁻ into Pt NPs (Figure d-g). The Pt/rGO catalysts have larger electrochemical surface area than Pt/C catalysts (1013.4 cm² mg⁻¹ vs 826.9 cm² mg⁻¹, calculated hydrogen adsorption region of CV curves), higher mass activity (333.3 mA mg⁻¹ vs 153.3 mA mg⁻¹ in acidic media; 552.5 mA mg⁻¹ vs 301.7 mA mg⁻¹ in alkaline media), higher poison tolerance ability (the ratio

I_f/I_b of peak current densities for the forward I_f and backward I_b : 7.45 vs 4.46), longer stability for methanol oxidation (85.6% vs 62.4% in acidic media; 77.9% vs 61.4% in alkaline media after 1000 cycles).^[125] Recently, they further enhanced the (Pt-load amount dependent) electrocatalytic performance of methanol oxidation using Pt/SnO₂/rGO nanocomposites which were constructed by photochemical reduction of PtCl₆²⁻ adsorbed on SnO₂ particles (Figure 10h).^[126] Very tiny 1~2 nm Pt NPs are uniformly dispersed on rGO nanosheets (Figure 10i). The mass activity is elevated up to 638.3 mA mg⁻¹ in acidic environment, lying among the excellent DMFCs reported so far.^[128] In addition, the methanol oxidation peak potential for the Pt_{0.89}/SnO₂/rGO catalysts is 0.615 V, 0.084 V lower than 0.699 V for the Pt/rGO catalysts, indicating easier oxygen-reduction reaction for Pt_{0.89}/SnO₂/rGO catalysts (Figure 10j). Pt/SnO₂/rGO catalysts also display higher stability than Pt/rGO, as confirmed by the 72.4% remaining peak current density after 1200 cycles for the former but 54.5% for the latter (Figure 10k-l).^[126] Well-dispersed small Pt NPs, smaller solid-state interfacial resistance originating from excellent conductivity of graphene, structural integrity from excellent stability of graphene are considered to lead to the excellent electrocatalytic performance of Pt/rGO and Pt/SnO₂/rGO catalysts. As for the higher activity of Pt/SnO₂/rGO over Pt/rGO composites, the synergetic effect between Pt and SnO₂ should be the key factor, which allows further oxidation of CO-like species during methanol oxidation following the reactions shown below.



Conclusion and Perspective

In summary, this decade has witnessed the rapid progress of applying laser-synthesized NMs for catalytic applications, which mainly benefit from a large diversity of one-step synthesized catalysts (e.g., monometallic, bimetallic, core-shell and defect-rich NPs) and their adaptability as the building blocks for complex catalysts development including ternary oxide, doped semiconductor, supported composite, NP-polymer and film catalysts with the aid of other techniques. In particular, the possibility of one-step synthesis of advanced catalysts (e.g., Au-FeOCl,^[129] Au-CoFe₂O₄,^[130] Au-SrTiO₃^[130]) under optimal conditions will bring great convenience to researchers. When it comes to the LAL/LPL-synthesized catalysts' properties, unique ligand-free of metallic and defect-rich of oxide catalysts endow the catalysts with more active sites and narrowed band gap, respectively, thus leading to their outstanding catalytic activities.^[63, 110] The highly surface charge and ligand-free features of LAL-synthesized catalysts facilitate the sufficient adsorption (up to almost 100%) of the nanocatalysts on various adsorbent supports,^[63] making them excellent candidates as adsorbants for assembling advanced heterogeneous supported catalysts. Some of the catalysts have reached the performance level comparable to or even higher than the commercial catalysts of P25 and Pt/C,^[87, 126] indicating their promising future as the next-generation commercial catalysts. Another appealing feature of this technique is the strength in one-step alloying transition-metals (e.g., Fe, Mn, Cu, Co, Ni, etc.) together or alloy them with noble

metals (Au and Pt) into cost-effective nanoalloys,^[11, 41, 51] which may greatly reduce the catalyst synthesis costs. It is well known that catalysts' performance depends on the catalysts' composition, morphology and size. Many challenges still exist for accurately manipulating the physical properties (size and morphology) and surface chemistry of the synthesized catalysts because of the difficulty in controlling the plasma generation-quenching processes. Jendrzej et al. have already observed the atom scale metallic clusters obtained by LPL, whose use for catalytic applications deserves expectation.^[16] Nevertheless, the coalescence and ripening of atom clusters in liquids certainly enlarge their size and deteriorate their activity. Hence, appropriate preservation methods (e.g., freezing) should be exploited to prevent their agglomeration or coalescence before put them into catalytic use. Deducing from the literature mentioned in this review, it is also clear that most the reported catalysts are metal-related catalysts, seldom about metal-free catalysts. Hence, future studies should also be done on investigating the feasibility of developing active metal-free catalysts using LAL/LPL.

Acknowledgements

This work was financially supported by the National Basic Research Program of China (2014CB931704), the National Natural Science Foundation of China (NSFC, no. 11304315, 51401206, 11404338, 51371166, 51571186, 11504375), and the CAS/SAFEA International Partnership Program for Creative Research Teams).

Reference

- [1] a) L. Mai, X. Tian, X. Xu, L. Chang and L. Xu, *Chem. Rev.* **2014**, *114*, 11828-11862; b) M. R. Hoffmann, S. T. Martin, W. Choi and D. W. Bahnemann, *Chem. Rev.* **1995**, *95*, 69-96; c) N. Nitta and G. Yushin, *Part. Part. Syst. Charact.* **2014**, *31*, 317-336; d) T. Montini, M. Melchionna, M. Monai and P. Fornasiero, *Chem. Rev.* **2016**, *116*, 5987-6041.
- [2] C.-J. Jia and F. Schuth, *Phys. Chem. Chem. Phys.* **2011**, *13*, 2457-2487.
- [3] Z. Niu and Y. Li, *Chem. Mater.* **2013**, *26*, 72-83.
- [4] J. A. Lopez-Sanchez, N. Dimitratos, C. Hammond, G. L. Brett, L. Kesavan, S. White, P. Miedziak, R. Tiruvalam, R. L. Jenkins and A. F. Carley, *Nat. Chem.* **2011**, *3*, 551-556.
- [5] a) F. Mafuné, J.-y. Kohno, Y. Takeda, T. Kondow and H. Sawabe, *J. Phys. Chem. B* **2001**, *105*, 5114-5120; b) A. Fojtik and A. Henglein, *Ber. Bunsenges. Phys. Chem.* **1993**, *97*, 252-254; c) J. Neddersen, G. Chumanov and T. M. Cotton, *Appl. Spectrosc.* **1993**, *47*, 1959-1964; d) J. Liu, C. Liang, Z. Tian, S. Zhang and G. Shao, *Sci. Rep.* **2013**, *3*, 1741.
- [6] a) A. V. Kabashin and M. Meunier, *J. Appl. Phys.* **2003**, *94*, 7941-7943; b) D. Zhang, B. Gökce, C. Notthoff and S. Barcikowski, *Sci. Rep.* **2015**, *5*, 13661.
- [7] G. Marzun, J. Nakamura, X. Zhang, S. Barcikowski and P. Wagener, *Appl. Surf. Sci.* **2015**, *348*, 75-84.
- [8] S. Scaramuzza, S. Agnoli and V. Amendola, *Phys. Chem. Chem. Phys.* **2015**, *17*, 28076-28087.
- [9] Y.-H. Chen and C.-S. Yeh, *Colloids Surf., A* **2002**, *197*, 133-139.
- [10] D. Zhang and B. Gökce, *Appl. Surf. Sci.* **2016**, *392*, 991-1003.
- [11] D. Zhang, Z. Ma, M. Spasova, A. E. Yelsukova, S. Lu, M. Farle, U. Wiedwald and B. Gökce, *Part. Part. Syst. Charact.* **2017**, *34*, 1600225.
- [12] M. Dell'Aglia, R. Gaudioso, O. De Pascale and A. De Giacomo, *Appl. Surf. Sci.* **2015**, *348*, 4-9.
- [13] D. Zhang, B. Gökce, S. Sommer, R. Streubel and S. Barcikowski, *Appl. Surf. Sci.* **2016**, *367*, 222-230.
- [14] S. Ibrahimkuty, P. Wagener, A. Menzel, A. Plech and S. Barcikowski, *Appl. Phys. Lett.* **2012**, *101*, 103104.
- [15] V. Amendola and M. Meneghetti, *Phys. Chem. Chem. Phys.* **2013**, *15*, 3027-3046.
- [16] S. Jendrzej, B. Gökce, V. Amendola and S. Barcikowski, *J. Colloid Interf. Sci.* **2016**, *463*, 299-307.
- [17] J. Liu, C. Liang, X. Zhu, Y. Lin, H. Zhang and S. Wu, *Sci. Rep.* **2016**, *6*, 32631.
- [18] C. Liang, T. Sasaki, Y. Shimizu and N. Koshizaki, *Chem. Phys. Lett.* **2004**, *389*, 58-63.
- [19] a) A. Takami, H. Kurita and S. Koda, *J. Phys. Chem. B* **1999**, *103*, 1226-1232; b) S. Link, C. Burda, B. Nikoobakht and M. A. El-Sayed, *J. Phys. Chem. B* **2000**, *104*, 6152-6163.
- [20] a) C. Liang, S. Wu, E. Dai, Y. Ye, J. Liu, Z. Tian, Y. Cai, X. Zhu and Y. Han, *ChemPhysChem* **2017**, DOI: 10.1002/cphc.201601185; b) D. Zhang, M. Lau, S. Lu, S. Barcikowski and B. Gökce, *Sci. Rep.* **2017**, *7*, 40355; c) H. Wang, N. Koshizaki, L. Li,

- L. Jia, K. Kawaguchi, X. Li, A. Pyatenko, Z. Swiatkowska-Warkocka, Y. Bando and D. Golberg, *Adv. Mater.* **2011**, *23*, 1865-1870; d) H. Wang, M. Miyauchi, Y. Ishikawa, A. Pyatenko, N. Koshizaki, Y. Li, L. Li, X. Li, Y. Bando and D. Golberg, *J. Am. Chem. Soc.* **2011**, *133*, 19102-19109.
- [21] K. Yamada, K. Miyajima and F. Mafuné, *J. Phys. Chem. C* **2007**, *111*, 11246-11251.
- [22] A. Pyatenko, H. Wang, N. Koshizaki and T. Tsuji, *Laser Photonics Rev.* **2013**, *7*, 596-604.
- [23] R.-C. Luo, C. Li, X.-W. Du and J. Yang, *Angew. Chem. Int. Ed.* **2015**, *54*, 4787-4791.
- [24] X. Chen, D. Zhao, K. Liu, C. Wang, L. Liu, B. Li, Z. Zhang and D. Shen, *ACS Appl. Mater. Interfaces* **2015**, *7*, 16070-16077.
- [25] H. J. Jung and M. Y. Choi, *J. Phys. Chem. C* **2014**, *118*, 14647-14654.
- [26] H. Zhang, S. Wu, J. Liu, Y. Cai and C. Liang, *Phys. Chem. Chem. Phys.* **2016**, *18*, 22503-22508.
- [27] A. Poletti, G. Fracasso, G. Conti, R. Pilot and V. Amendola, *Nanoscale* **2015**, 13702-13714.
- [28] W. Li, X. Ge, H. Zhang, Q. Ding, H. Ding, Y. Zhang, G. Wang, H. Zhang and H. Zhao, *Inorg. Chem. Front.* **2016**, *3*, 663-670.
- [29] C. A. Schaumberg, M. Wollgarten and K. Rademann, *J. Phys. Chem. A* **2014**, *118*, 8329-8337.
- [30] H. Zeng, X. W. Du, S. C. Singh, S. A. Kulinich, S. Yang, J. He and W. Cai, *Adv. Funct. Mater.* **2012**, *22*, 1333-1353.
- [31] D. Wang and Y. Li, *Adv. Mater.* **2011**, *23*, 1044-1060.
- [32] R. Ferrando, J. Jellinek and R. L. Johnston, *Chem. Rev.* **2008**, *108*, 845-910.
- [33] G. Marzun, A. Levish, V. Mackert, T. Kallio, S. Barcikowski and P. Wagener, *J. Colloid Interf. Sci.* **2017**, *489*, 57-67.
- [34] a) S. b. Besner and M. Meunier, *J. Phys. Chem. C* **2010**, *114*, 10403-10409; b) J. Zhang, J. Worley, S. Dénommée, C. Kingston, Z. J. Jakubek, Y. Deslandes, M. Post, B. Simard, N. Braidly and G. A. Botton, *J. Phys. Chem. B* **2003**, *107*, 6920-6923.
- [35] P. Wagener, J. Jakobi, C. Rehbock, V. S. K. Chakravadhanula, C. Thede, U. Wiedwald, M. Bartsch, L. Kienle and S. Barcikowski, *Sci. Rep.* **2016**, *6*, 23352.
- [36] K. D. Malviya and K. Chattopadhyay, *J. Phys. Chem. C* **2016**, *120*, 27699-27706.
- [37] K. D. Malviya and K. Chattopadhyay, *J. Phys. Chem. C* **2014**, *118*, 13228-13237.
- [38] A. Neumeister, J. Jakobi, C. Rehbock, J. Moysig and S. Barcikowski, *Phys. Chem. Chem. Phys.* **2014**, *16*, 23671-23678.
- [39] J. Zhang, G. Chen, D. Guay, M. Chaker and D. Ma, *Nanoscale* **2014**, *6*, 2125-2130.
- [40] D. N. Oko, S. Garbarino, J. Zhang, Z. Xu, M. Chaker, D. Ma, D. Guay and A. C. Tavares, *Electrochim. Acta* **2015**, *159*, 174-183.
- [41] Z. Lin, J. Li, L. Li, L. Yu, W. Li and G. Yang, *J. Mater. Chem. A* **2017**, *5*, 773-781.
- [42] H. Zhang, C. Liang, J. Liu, Z. Tian and G. Shao, *Carbon* **2013**, *55*, 108-115.
- [43] H. Zhang, J. Liu, Z. Tian, Y. Ye, Y. Cai, C. Liang and K. Terabe, *Carbon* **2016**,

100, 590-599.

- [44] R. Ghosh Chaudhuri and S. Paria, *Chem. Rev.* **2011**, *112*, 2373-2433.
- [45] D. S. Su, S. Perathoner and G. Centi, *Chem. Rev.* **2013**, *113*, 5782-5816.
- [46] S. Yang, W. Cai, H. Zhang, H. Zeng and Y. Lei, *J. Phys. Chem. C* **2011**, *115*, 7279-7284.
- [47] R. G. Calzada, K. Bagga, P. Bianchini, V. Chirvony and J. P. Martínez-Pastor, *RSC Adv.* **2015**, *5*, 50604–50610.
- [48] D. Wang, H. Zhang, L. Li, M. Chen and X. Liu, *Opt. Mater. Express* **2016**, *6*, 1306-1312.
- [49] a) H. Zeng, W. Cai, P. Liu, X. Xu, H. Zhou, C. Klingshirn and H. Kalt, *ACS Nano* **2008**, *2*, 1661-1670; b) H. Zeng, P. Liu, W. Cai, S. Yang and X. Xu, *J. Phys. Chem. C* **2008**, *112*, 19620-19624.
- [50] V. Amendola, P. Riello and M. Meneghetti, *J. Phys. Chem. C* **2011**, *115*, 5140-5146.
- [51] V. Amendola, S. Scaramuzza, F. Carraro and E. Cattaruzza, *J. Colloid Interf. Sci.* **2016**, *489*, 18-27.
- [52] P. Munnik, P. E. de Jongh and K. P. de Jong, *Chem. Rev.* **2015**, *115*, 6687-6718.
- [53] M. Liu, R. Zhang and W. Chen, *Chem. Rev.* **2014**, *114*, 5117-5160.
- [54] R. S. Sai Siddhardha, V. Lakshman Kumar, A. Kaniyoor, V. Sai Muthukumar, S. Ramaprabhu, R. Podila, A. M. Rao and S. S. Ramamurthy, *Spectrochim. Acta, Part A* **2014**, *133*, 365-371.
- [55] P. Wang, Y. Ye, D. Liang, H. Sun, J. Liu, Z. Tian and C. Liang, *RSC Adv.* **2016**, *6*, 26977-26983.
- [56] R. Singh and R. K. Soni, *J. Nanosci. Nanotechnol.* **2014**, *14*, 6872-6879.
- [57] R. Ma, Y.-j. Kim, D. Amaranatha Reddy and T. K. Kim, *Ceram. Int.* **2015**, *41*, 12432-12438.
- [58] K. B. Cederquist, B. Liu, M. R. Grima, P. J. Dalack and J. T. Mahorn, *Colloids Surf. B Biointerfaces* **2017**, *149*, 351-357.
- [59] S. Li, J. Zhang, M. G. Kibria, Z. Mi, M. Chaker, D. Ma, R. Nechache and F. Rosei, *Chem. Commun.* **2013**, *49*, 5856-5858.
- [60] S. Hebié, Y. Holade, K. Maximova, M. Sentis, P. Delaporte, K. B. Kokoh, T. W. Napporn and A. V. Kabashin, *ACS Catal.* **2015**, *5*, 6489-6496.
- [61] S. Gu, J. Kaiser, G. Marzun, A. Ott, Y. Lu, M. Ballauff, A. Zacccone, S. Barcikowski and P. Wagener, *Catal. Lett.* **2015**, *145*, 1105-1112.
- [62] S. Gu, S. Wunder, Y. Lu, M. Ballauff, R. Fenger, K. Rademann, B. Jaquet and A. Zacccone, *J. Phys. Chem. C* **2014**, *118*, 18618-18625.
- [63] J. Zhang, G. Chen, M. Chaker, F. Rosei and D. Ma, *Appl. Catal., B* **2013**, *132*, 107-115.
- [64] T. M. Riddick in *Zeta-Meter Operating Manual zm-75*, Zeta-Meter, Vol. Inc. New York, **1968**.
- [65] a) H. He, W. Cai, Y. Lin and B. Chen, *Langmuir* **2010**, *26*, 8925-8932; b) M. A. Sobhan, M. J. Withford and E. M. Goldys, *Langmuir* **2009**, *26*, 3156-3159; c) D. Werner, S. Hashimoto, T. Tomita, S. Matsuo and Y. Makita, *J. Phys. Chem. C* **2008**, *112*, 16801-16808; d) J.-P. Sylvestre, S. Poulin, A. V. Kabashin, E. Sacher, M.

- Meunier and J. H. T. Luong, *J. Phys. Chem. B* **2004**, *108*, 16864-16869.
- [66] N. Bärsch, J. Jakobi, S. Weiler and S. Barcikowski, *Nanotechnology* **2009**, *20*, 445603.
- [67] a) H. Zhang, C. Liang, J. Liu, Z. Tian, G. Wang and W. Cai, *Langmuir* **2012**, *28*, 3938-3944; b) T. Tsuji, M. Nakanishi, T. Mizuki, M. Tsuji, T. Doi, T. Yahiro and J. Yamaki, *Appl. Surf. Sci.* **2009**, *255*, 9626-9629; c) S. S. Pan, W. Lu, Y. H. Zhao, W. Tong, M. Li, L. M. Jin, J. Y. Choi, F. Qi, S. G. Chen, L. F. Fei and S. F. Yu, *ACS Appl. Mater. Interfaces* **2013**, *5*, 12784-12788.
- [68] H. Bao, Y. Wang, H. Zhang, Q. Zhao, G. Liu and W. Cai, *J. Colloid Interf. Sci.* **2017**, *489*, 92-99.
- [69] C. He, T. Sasaki, H. Usui, Y. Shimizu and N. Koshizaki, *J. Photochem. Photobiol., A* **2007**, *191*, 66-73.
- [70] C. Rehbock, V. Merk, L. Gamrad, R. Streubel and S. Barcikowski, *Phys. Chem. Chem. Phys.* **2013**, *15*, 3057-3067.
- [71] V. Merk, C. Rehbock, F. Becker, U. Hagemann, H. Nienhaus and S. Barcikowski, *Langmuir* **2014**, *30*, 4213-4222.
- [72] C. Pfeiffer, C. Rehbock, D. Hühn, C. Carrillo-Carrion, D. J. de Aberasturi, V. Merk, S. Barcikowski and W. J. Parak, *J. R. Soc. Interface* **2014**, *11*, 20130931.
- [73] H. Muto, K. Yamada, K. Miyajima and F. Mafuné, *J. Phys. Chem. C* **2007**, *111*, 17221-17226.
- [74] C. Streich, S. Koenen, M. Lelle, K. Peneva and S. Barcikowski, *Appl. Surf. Sci.* **2015**, *348*, 92-99.
- [75] a) J. Schneider, M. Matsuoka, M. Takeuchi, J. Zhang, Y. Horiuchi, M. Anpo and D. W. Bahnemann, *Chem. Rev.* **2014**, *114*, 9919-9986; b) U. Diebold, *Surf. Sci. Rep.* **2003**, *48*, 53-229.
- [76] I. Justicia, P. Ordejon, G. Canto, J. L. D. L. M. D. L. Mozos, J. Fraxedas, G. A. Battiston, R. Gerbasi and A. Figueras, *Adv. Mater.* **2002**, *14*, 1399-1402.
- [77] Z. Zhang and J. T. Yates, *Chem. Rev.* **2012**, *112*, 5520-5551.
- [78] L. Li, L. Yu, Z. Lin and G. Yang, *ACS Appl. Mater. Interfaces* **2016**, *8*, 8536-8545.
- [79] a) C. Liang, Y. Shimizu, T. Sasaki and N. Koshizaki, *J. Phys. Chem. B* **2003**, *107*, 9220-9225; b) Z. Tian, C. Liang, J. Liu, H. Zhang and L. Zhang, *J. Mater. Chem.* **2011**, *21*, 18242-18247.
- [80] J. Liu, C. Liang, H. Zhang, Z. Tian and S. Zhang, *J. Phys. Chem. C* **2012**, *116*, 4986-4992.
- [81] Y. Ye, P. Wang, E. Dai, J. Liu, Z. Tian, C. Liang and G. Shao, *Phys. Chem. Chem. Phys.* **2014**, *16*, 8801-8807.
- [82] L. Li, Z. Deng, J. Xiao and G. Yang, *Nanotechnology* **2015**, *26*, 255705.
- [83] Y. Yu, H. J. Jung, M. Je, H. C. Choi and M. Y. Choi, *Chemosphere* **2016**, *155*, 250-256.
- [84] Y. Zhang, L. Li, H. Su, W. Huang and X. Dong, *J. Mater. Chem. A* **2015**, *3*, 43-59.
- [85] M. V. Reddy, G. V. Subba Rao and B. V. R. Chowdari, *Chem. Rev.* **2013**, *113*, 5364-5457.

- [86] M. Rui, X. Li, L. Gan, T. Zhai and H. Zeng, *Adv. Funct. Mater.* **2016**, DOI: 10.1002/adfm.201600785.
- [87] Z. Tian, C. Liang, J. Liu, H. Zhang and L. Zhang, *J. Mater. Chem.* **2012**, *22*, 17210-17214.
- [88] S. Wu, P. Wang, Y. Cai, D. Liang, Y. Ye, Z. Tian, J. Liu and C. Liang, *RSC Adv.* **2015**, *5*, 9069-9074.
- [89] Z. Tian, S. Wu, P. Wang, Y. Cai, D. Liang, Y. Ye, J. Liu and C. Liang, *CrystEngComm* **2015**, *17*, 3015-3022.
- [90] D. Liang, S. Wu, P. Wang, Y. Cai, Z. Tian, J. Liu and C. Liang, *RSC Adv.* **2014**, *4*, 26201-26206.
- [91] a) Z. Zhou, P. Huo, L. Guo and O. V. Prezhdo, *J. Phys. Chem. C* **2015**, *119*, 26303-26310; b) S. Kumari, A. P. Singh, C. Tripathi, D. Chauhan, S. Dass, R. Shrivastav, V. Gupta, K. Sreenivas and V. R. Satsangi, *Int. J. Photoenergy* **2007**, *2007*, 87467.
- [92] a) J. Liu, C. Liang, G. Xu, Z. Tian, G. Shao and L. Zhang, *Nano Energy* **2013**, *2*, 328-336; b) J. Liu, C. Liang, H. Zhang, S. Zhang and Z. Tian, *Chem. Commun.* **2011**, *47*, 8040-8042.
- [93] J. Liu, Y. Y. Cai, Z. F. Tian, G. S. Ruan, Y. X. Ye, C. H. Liang and G. S. Shao, *Nano Energy* **2014**, *9*, 282-290.
- [94] G. Ruan, S. Wu, P. Wang, J. Liu, Y. Cai, Z. Tian, Y. Ye, C. Liang and G. Shao, *RSC Adv.* **2014**, *4*, 63408-63413.
- [95] Z. Xu, M. Quintanilla, F. Vetrone, A. O. Govorov, M. Chaker and D. Ma, *Adv. Funct. Mater.* **2015**, *25*, 2950-2960.
- [96] T. A. Saleh, M. Gondal and Q. Drmosh, *Nanotechnology* **2010**, *21*, 495705.
- [97] W. Dong, S. Reichenberger, S. Chu, P. Weide, H. Ruland, S. Barcikowski, P. Wagener and M. Muhler, *J. Catal.* **2015**, *330*, 497-506.
- [98] P. Wagener, A. Schwenke and S. Barcikowski, *Langmuir* **2012**, *28*, 6132-6140.
- [99] G. Marzun, C. Streich, S. Jendrzey, S. Barcikowski and P. Wagener, *Langmuir* **2014**, *30*, 11928-11936.
- [100] J. Zhang, D. Han, H. Zhang, M. Chaker, Y. Zhao and D. Ma, *Chem. Commun.* **2012**, *48*, 11510-11512.
- [101] a) W. Guo and B. Liu, *ACS Appl. Mater. Interfaces* **2012**, *4*, 7036-7042; b) V. Svrcek, D. Mariotti, T. Nagai, Y. Shibata, I. Turkevych and M. Kondo, *J. Phys. Chem. C* **2011**, *115*, 5084-5093.
- [102] S. D. Angelov, S. Koenen, J. Jakobi, H. E. Heissler, M. Alam, K. Schwabe, S. Barcikowski and J. K. Krauss, *J. Nanobiotechnol.* **2016**, *14*, 3.
- [103] P. Kalita, J. Singh, M. K. Singh, P. R. Solanki, G. Sumana and B. Malhotra, *Appl. Phys. Lett.* **2012**, *100*, 093702.
- [104] X. Xu, G. Duan, Y. Li, G. Liu, J. Wang, H. Zhang, Z. Dai and W. Cai, *ACS Appl. Mater. Interfaces* **2013**, *6*, 65-71.
- [105] S. Wang, K. Dou, Y. Zou, Y. Dong, J. Li, D. Ju and H. Zeng, *J. Colloid Interf. Sci.* **2017**, *489*, 85-91.
- [106] E. Pizzolato, S. Scaramuzza, F. Carraro, A. Sartori, S. Agnoli, V. Amendola, M. Bonchio and A. Sartorel, *J. Energy Chem.* **2016**, *25*, 246-250.

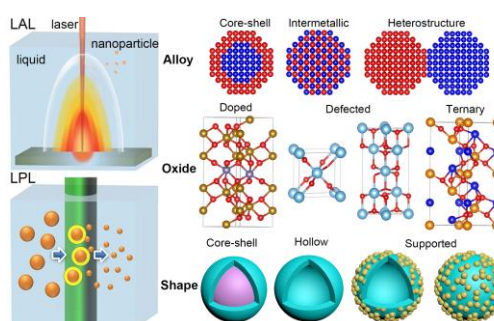
- [107] a) Z. Li, C. Dong, J. Yang, S. Qiao and X. Du, *J. Mater. Chem. A* **2016**, 2699-2704; b) J. Xiao, P. Liu, Y. Liang, H. B. Li and G. W. Yang, *J. Appl. Phys.* **2013**, *114*, 073513.
- [108] H. Zhang, J. Liu, Y. Ye, Z. Tian and C. Liang, *Phys. Chem. Chem. Phys.* **2013**, *15*, 5684-5690.
- [109] a) M. Zimbone, M. A. Bucchini, G. Cacciato, R. Sanz, G. Rappazzo, S. Boninelli, R. Reitano, L. Romano, V. Privitera and M. G. Grimaldi, *Appl. Catal., B* **2015**, *165*, 487-494; b) M. A. Pugachevskii, *Nanosci. Nanotechnol. Lett.* **2014**, *6*, 519-523; c) M. Zimbone, G. Cacciato, M. A. Bucchini, R. Sanz, N. Piluso, R. Reitano, F. La Via, M. G. Grimaldi and V. Privitera, *Mat. Sci. Semicon. Proc.* **2016**, *42*, 28-31; d) P. Liu, W. Cai, M. Fang, Z. Li, H. Zeng, J. Hu, X. Luo and W. Jing, *Nanotechnology* **2009**, *20*, 285707.
- [110] Z. Lin, J. Li, Z. Zheng, J. Yan, P. Liu, C. Wang and G. Yang, *ACS Nano* **2015**, *9*, 7256-7265.
- [111] J. Xiao, Q. L. Wu, P. Liu, Y. Liang, H. B. Li, M. M. Wu and G. W. Yang, *Nanotechnology* **2014**, *25*, 135702.
- [112] Q. Li, C. Liang, Z. Tian, J. Zhang, H. Zhang and W. Cai, *CrystEngComm* **2012**, *14*, 3236-3240.
- [113] M. A. Gondal, A. M. Ilyas and U. Baig, *Ceram. Inter.* **2016**, *42*, 13151-13160.
- [114] Y. Cai, Y. Ye, Z. Tian, J. Liu, Y. Liu and C. Liang, *Phys. Chem. Chem. Phys.* **2013**, *15*, 20203-20209.
- [115] Z. Wang, Z. Wang, D. Wang and M. Chen, *RSC Adv.* **2016**, *6*, 12286-12289.
- [116] H. Zhang, C. Liang, Z. Tian, J. Liu and W. Cai, *CrystEngComm* **2011**, *13*, 4676-4682.
- [117] F. Zuo, L. Wang, T. Wu, Z. Zhang, D. Borchardt and P. Feng, *J. Am. Chem. Soc.* **2010**, *132*, 11856-11857.
- [118] J. Ran, J. Zhang, J. Yu, M. Jaroniec and S. Z. Qiao, *Chem. Soc. Rev.* **2014**, *43*, 7787-7812.
- [119] S. Filice, G. Compagnini, R. Fiorenza, S. Scirè, L. D'Urso, M. E. Fragalà, P. Russo, E. Fazio and S. Scalese, *J. Colloid Interf. Sci.* **2017**, *489*, 131-137.
- [120] L. Liao, Q. Zhang, Z. Su, Z. Zhao, Y. Wang, Y. Li, X. Lu, D. Wei, G. Feng and Q. Yu, *Nat. Nanotechnol.* **2014**, *9*, 69-73.
- [121] J. D. Blakemore, H. B. Gray, J. R. Winkler and A. M. Müller, *ACS Catal.* **2013**, *3*, 2497-2500.
- [122] B. M. Hunter, H. B. Gray and A. M. Müller, *Chem. Rev.* **2016**, *116*, 14120-14136.
- [123] S. Hu, M. Tian, E. L. Ribeiro, G. Duscher and D. Mukherjee, *J. Power Sources* **2016**, *306*, 413-423.
- [124] B. M. Hunter, J. D. Blakemore, M. Deimund, H. B. Gray, J. R. Winkler and A. M. Müller, *J. Am. Chem. Soc.* **2014**, *136*, 13118-13121.
- [125] S. Wu, J. Liu, Z. Tian, Y. Cai, Y. Ye, Q. Yuan and C. Liang, *ACS Appl. Mater. Interfaces* **2015**, *7*, 22935-22940.
- [126] S. Wu, J. Liu, D. Liang, H. Sun, Y. Ye, Z. Tian and C. Liang, *Nano Energy* **2016**, *26*, 699-707.

- [127] D. S. Falcão, V. B. Oliveira, C. M. Rangel and A. M. F. R. Pinto, *Renew. Sust. Energy Rev.* **2014**, *34*, 58-70.
- [128] H. Huang and X. Wang, *J. Mater. Chem. A* **2014**, *2*, 6266-6291.
- [129] Y. Wang, H. Zhang, Y. Zhu, Z. Dai, H. Bao, Y. Wei and W. Cai, *Adv. Mater. Interfaces* **2016**, DOI: 10.1002/admi.201500801.
- [130] J. L. Guo, Y. D. Chiou, W. I. Liang, H. J. Liu, Y. J. Chen, W. C. Kuo, C. Y. Tsai, K. A. Tsai, H. H. Kuo and W. F. Hsieh, *Adv. Mater.* **2013**, *25*, 2040-2044.

Entry for the Table of Contents (Please choose one layout)

FOCUS REVIEW

This focus review shows the strength of a new technique — laser ablation/processing in liquids — in one-step synthesis of ligand-free catalysts without any surfactant additive as well as its excellence at defect introduction to semiconductor photocatalysts.



Dongshi Zhang, Jun Liu, Pengfei Li,
Zhenfei Tian, Changhao Liang*

Page No. – Page No.

**Recent Advances in Ligand-Free,
Charged and Defect-Rich Catalysts
Developed by Laser Ablation and
Processing in Liquids**



Dr. Dongshi Zhang obtained Ph.D. from Xi'an Jiaotong University (China) in 2014 and worked in Prof. Stephan Barcikowski group at University of Duisburg-Essen (Germany) from 2014 to 2016. Currently, he works in Prof. Changhao Liang group to further his researches. His research interests include laser ablation, laser microfabrication, and laser cutting as well as their combination with surface chemistry for wettability control and with inorganic chemistry for novel nanomaterial synthesis.



Changhao Liang obtained his Ph.D. from Institute of Solid State Physics, Chinese Academy of Sciences in 2001. He is currently a full professor in Laboratory of Nanostructured Materials, Institute of Solid State Physics. His current research interest lies in laser-materials interactions in liquids, nanoionics-based resistive switching devices, nanomaterials for energy & environmental applications.